Measurements of ^{12}C ions fragmentation cross sections on thin targets with the FIRST apparatus.

Z. Abou-Haidar,[a] C. Agodi,[b] M.A.G. Alvarez,[a] T. Aumann,[c] F. Balestra,[d] G. Battistoni,[e] A. Bocci,[a] T.T. Böhlen,[f] A. Boudard,[g] A. Brunetti,[h] M. Carpinelli,[h] G.A.P. Cirrone,[b] M.A. Cortes-Giraldo,[i] G. Cuttone,[b] M. De Napoli,[j] M. Durante,[c] J.P. Fernández-García,[k] Ch. Finck,[l] B. Golosio,[h] E. Iarocci,[m] F. Iazzi,[d] G. Ickert,[c] R. Introzzi,[d] D. Juliani,[l] J. Krimmer,[n] A.H. Kummali,[o] N. Kurz,[c] M. Labalme,[p] Y. Leifels,[c] A. Le Fevre,[c] S. Leray,[g] F. Marchetto,[q] V. Monaco,[o] M.C. Morone,[r] D. Nicolosi,[s] P. Oliva,[h] A. Paoloni,[t] V. Patera,[u] L. Piersanti,[u] R. Pleskac,[c] N. Randazzo,[j] R. Rescigno,[l] F. Romano,[v] D. Rossi,[c] V. Rosso,[w] M. Rousseau,[l] R. Sacchi,[o] P. Sala,[e] S. Salvador,[p] A. Sarti,[m] C. Scheidenberger,[c] C. Schuy,[c] A. Sciubba,[u] C. Sfienti,[x] H. Simon,[c] V. Sipala,[y] E. Spiriti,[z] M. Toppi,[aa] S. Tropea,[b] M. Vanstalle,[l] and H. Younis[bb]

(The FIRST Collaboration)

(Dated: December 15, 2014)

A detailed knowledge of the heavy ions interaction processes with matter is of great interest in basic and applied physics. As an example, particle therapy and space radioprotection require highly accurate fragmentation cross section measurements to develop shielding materials, estimate acute and late health risks for manned missions in space and for treatment planning in particle therapy.

The FIRST (Fragmentation of Ions Relevant for Space and Therapy) experiment at the Helmholtz Center for Heavy Ion research (GSI) was designed and built by an international collaboration from France, Germany, Italy and Spain for studying the collisions of a ^{12}C ion beam with carbon and gold thin targets. The experiment main purpose is to provide the first measurement of double differential cross section measurement of carbon ion fragmentation at energies that are relevant both for tumor therapy and space radiation protection applications. The SIS (heavy ion synchrotron) was used to accelerate the ^{12}C ions at the energy of 400 MeV/u: this energy is particularly interesting for particle therapy applications, where ^{12}C ions of such an energy are used for the treatment of deep seated tumors.

This paper presents the single differential fragmentation cross section, measured as a function of the fragments angle and kinetic energy. The impact on the applied fields relevant for such studies as well as the comparison with other published data in similar conditions will be also presented.

[a] CNA, Sevilla, Spain
[b] Istituto Nazionale di Fisica Nucleare - Laboratori Nazionali del Sud, Italy
[c] GSI Helmholtzzentrum fur Schwerionenforschung, Darmstadt, Germany
[d] Istituto Nazionale di Fisica Nucleare - Sezione di Torino, Italy; Dipartimento di Fisica, Politecnico di Torino, Italy
[e] Istituto Nazionale di Fisica Nucleare - Sezione di Milano, Italy
[f] European Organization for Nuclear Research CERN, Geneva, Switzerland; Medical Radiation Physics, Karolinska Institutet and Stockholm University, Stockholm, Sweden
[g] CEA-Saclay, IRFU/SPhN, Gif sur Yvette Cedex, France
[h] Istituto Nazionale di Fisica Nucleare - Sezione di Cagliari, Italy; Universita' di Sassari, Italy
[i] Departamento de Fisica Atomica, Molecular y Nuclear, University of Sevilla, 41080-Sevilla, Spain
[j] Istituto Nazionale di Fisica Nucleare - Sezione di Catania, Italy
[k] Departamento de Física Atómica, Molecular y Nuclear, University of Sevilla, 41080-Sevilla, Spain
[l] IPHC, Université de Strasbourg, CNRS, UMR7178, 67037 Strasbourg, France
[m] Istituto Nazionale di Fisica Nucleare - Laboratori Nazionali di Frascati, Italy; Dipartimento di Scienze di Base e Applicate per l'Ingegneria, "La Sapienza" Università di Roma, Italy
[n] IPN-Lyon, Universite de Lyon, Universite Lyon 1, CNRS/IN2P3, Villeurbanne, France
[o] Istituto Nazionale di Fisica Nucleare - Sezione di Torino, Italy; Dipartimento di Fisica, Universita' di Torino, Italy
[p] LPC-Caen, ENSICAEN, Université de Caen, CNRS/IN2P3, Caen, France
[q] Istituto Nazionale di Fisica Nucleare - Sezione di Torino, Italy
[r] Istituto Nazionale di Fisica Nucleare - Sezione di Roma Tor Vergata, Italy; Dipartimento di Biopatologia e Diagnostica per Immagini, Universita' di Roma Tor Vergata, Italy
[s] Dipartimento di Fisica, Universitá di Catania, Italy; Istituto Nazionale di Fisica Nucleare - Laboratori Nazionali del Sud, Italy
[t] Istituto Nazionale di Fisica Nucleare - Laboratori Nazionali di Frascati, Italy
[u] Istituto Nazionale di Fisica Nucleare - Sezione di Roma 1, Italy; Dipartimento di Scienze di Base e Applicate per l'Ingegneria, "La Sapienza" Università di Roma, Italy
[v] Istituto Nazionale di Fisica Nucleare - Laboratori Nazionali del Sud, Italy; Centro Studi e Ricerche e Museo Storico della Fisica "Enrico Fermi", Roma, Italy
[w] Dipartimento di Fisica, Universitá di Pisa, Italy; Istituto Nazionale di Fisica Nucleare - Sezione di Pisa, Italy
[x] Istituto Nazionale di Fisica Nucleare - Laboratori Nazionali del Sud, Italy; Medical Radiation Physics, Karolinska Institutet and Stockholm University, Stockholm, Sweden
[y] Istituto Nazionale di Fisica Nucleare - Sezione di Cagliari, Italy
[z] Istituto Nazionale di Fisica Nucleare - Laboratori Nazionali di Frascati, Italy; Istituto Nazionale di Fisica Nucleare - Sezione di Roma 3, Italy
[aa] Istituto Nazionale di Fisica Nucleare - Laboratori Nazionali di Frascati, Italy; Dipartimento di Fisica, Universitá di Roma Tor Vergata, Italy
[bb] Department of Physics COMSATS Institute of Information Technology, Islamabad Pakistan

I. INTRODUCTION

The study of the mechanisms underlying the ion fragmentation in collisions at energies in the 10-1000 MeV/u range has been already object in the past of several experimental campaigns, either aiming at thin or thick target single or double differential cross section (DDCS) measurements [1–6]. Such measurements have been performed in different experimental conditions, covering in some cases only the very forward fragment emission region and in other cases few other fixed target angle configurations. Recently a double differential cross section measurement in thin targets has been performed using ^{12}C ions of 95 MeV/u kinetic energy as projectiles, with an experimental setup able to cover a large angular range: 0° [7] and 4°-45° [8].

The interest in such measurements is driven by the possible use in space [9, 10] and particle therapy applications [11, 12] of an improved description of the heavy ions interactions with matter. In particular, for both applications, one of the most interesting ion type/energy range pair to be explored is ^{12}C in the 200−1000 MeV/u range: cross section measurements using thin targets are needed in order to provide the missing information in the nuclear fragmentation databases, as NASA recently pointed out [13]. Deep seated tumors particle therapy with ^{12}C ions is indeed spanning this energy range and a better understanding of the fragmentation of a carbon beam inside a patient will allow a better treatment planning. The dose monitoring for such treatments would benefit as well from the improved DDCS measurements: secondary proton interaction vertex imaging has been shown to provide online control of the range during carbon therapy [14] and the precision of the method relies strongly on the knowledge of protons production DDCS [15].

The FIRST (Fragmentation of Ions Relevant for Space and Therapy) collaboration principal aim is to perform double differential cross section measurements (DDCS) using fully stripped ^{12}C ions as projectiles on thin targets of carbon, gold and other materials in the energy range not yet covered by other experiments [16]. The data taking took place in the GSI laboratory (Darmstadt) in 2011 summer and about 25 (5) million events of collisions between a ^{12}C ion beam with a thin carbon (gold) target were recorded.

The experimental setup, which included a trigger counter, a beam monitor, a vertex pixel detector, a plastic scintillator calorimeter and a time of flight wall (TW) made of plastic scintillators, is fully described in section II, together with the experiment Data AcQuisition (DAQ) system. The performances obtained by the various subdetectors are outlined together with their calibration strategies and results.

Details on the data sample and on the MonteCarlo (MC) simulation are given in section III, the description of the global reconstruction algorithms that have been used to fully reconstruct all the fragments and particles traversing the detector in each event can be found in section IV, while the results are presented in section V. The studies performed to assess the systematic uncertainty are documented in section VI.

The impact of the obtained results for particle therapy applications, as well as some considerations about the future developments of the still ongoing data analysis are finally discussed in section VII.

II. EXPERIMENTAL SETUP

Fragmentation cross sections are measured in FIRST using an experimental setup, already described in [16], that has been designed and optimized using a dedicated MC simulation. The schematic view of the FIRST experimental setup is shown in Fig.1, together with the axis orientation of the reference frame.

The detection of the incoming ^{12}C ions has been accomplished by means of a Start Counter (SC), described in detail in § II A, made of a thin layer of plastic scintillator whose geometry and read-out were optimized in order to maximize the counting efficiency while keeping the pre-target fragmentation as low as possible. The SC was used to trigger the data acquisition using a minimum bias strategy: whenever a ^{12}C ion was detected inside the SC the event was acquired.

A pixel silicon detector (VTX), described in detail in § II C, was placed just behind the target, allowing a precise reconstruction of the fragments produced in the target and their angle with respect to the incoming beam direction, as well as their production vertex. The technology adopted for the vertex detectors [17, 18] allowed to have the required efficiency with extra thin detection layers that minimized the out-of-target fragmentation of an elastically scattered ^{12}C ion or other heavy fragments coming out from the target.

The long read-out time of the pixel detector, with an incoming beam rate in the 1-10 kHz range, required the development of a dedicated fast Beam Monitor (BM) detector, capable of resolving the event Pile Up (PU) ambiguity in the VTX by providing the position of the impinging ^{12}C ion in the target. The technology chosen and the performances of such detector are presented in § II B.

A plastic scintillator calorimeter (Kinetic ENergy and Time Resolution Optimized on Scintillator, KENTROS) has been used to detect fragments, mainly protons and heliums, emitted at large angles. This detector surrounds the target and vertex detector region covering the azimuthal angle (defined as the angle between the incoming ^{12}C ion and the fragment direction) region between 5° and 90°. The results obtained in that region are not presented here and will be subject of a dedicated paper in the future, where a fully detailed description of the detector technology will be published.

The charged fragment momentum is computed by measuring the bending of the trajectory in the z-x plane induced by the magnetic field provided by the ALADIN

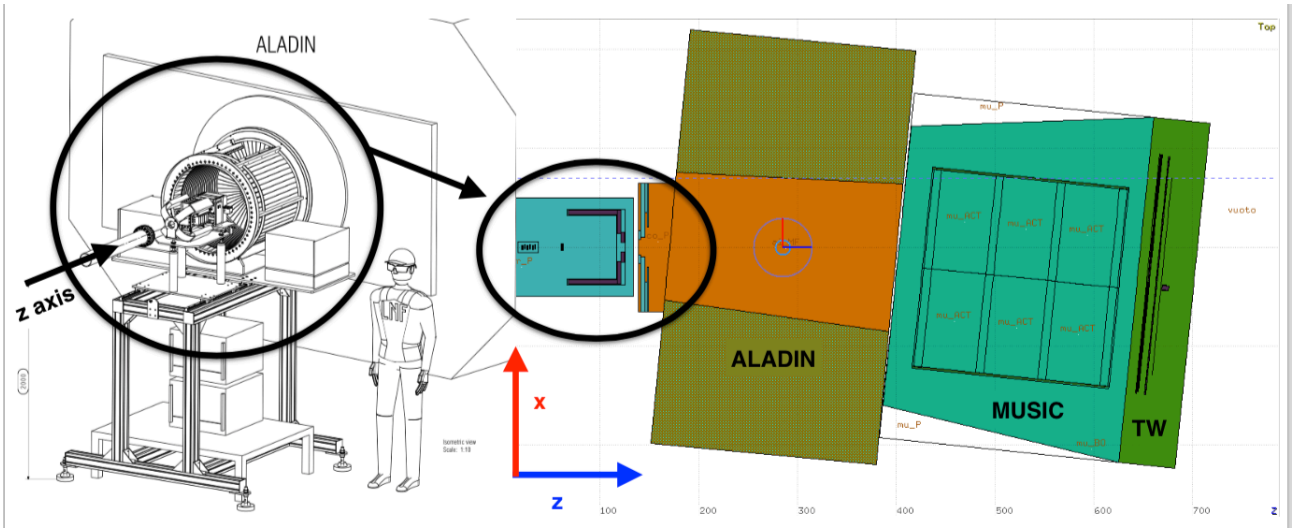

FIG. 1. Top view (x,z plane) of the FIRST experiment. From left to right: the beam pipe after the last collimator and the beam exit window; the table supporting the SC, the BM and the VTX detectors, enclosing the target holder; the KENTROS calorimeter, just before the magnet entrance window; the ALADIN magnet region; the TW detector at the right most position.

magnet, whose description is reported in § II D.

The fragment identification and energy measurement are performed using scintillating detectors placed six meters away from the target region, arranged in a wall (TW), described in § II E. Together with the time of flight (ToF) measurement, TW provides the detected fragment coordinates and a measurement of the energy released inside the plastic scintillators: this information allows, when combined, a clean separation of fragments with different charge.

An additional detector, a large volume time projection chamber (TP-MUSIC IV [19]), was placed after the ALADIN magnet and before the TW, but could not be operated during the datataking: the experiment full simulation takes this detector into account in order to properly evaluate the material traversed by each fragment before reaching the TW and account for a possible secondary fragmentation.

A. Start Counter Detector

The SC detector is used in FIRST to provide a measurement of the total number of ^{12}C ions used for the cross section evaluation and the trigger signal for the data acquisition system. The SC, shown in Fig. 2, also provides the reference time for all the other detectors, allowing the measurement of the drift time inside the BM, and of the fragment ToF using the TW information. The layout optimization, described in detail in [20], was hence performed carefully balancing the detector time resolution and the thickness minimization, in order to have a pre–target particle interaction probability that is less than 1% with respect to the on–target one.

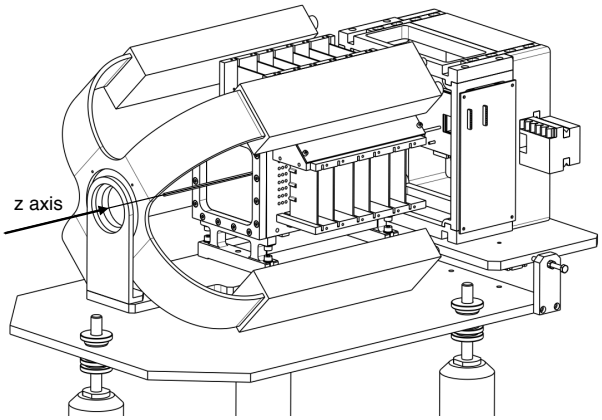

FIG. 2. Schematic view of the mechanical installation of SC and BM detectors. The picture shows the BM, with six wire planes on both xz and yz views, encapsulated by the SC mechanical structure. The four arms of the SC, holding the fibers and the PMTs used for the read-out can be clearly seen. The beam (z) axis is also shown, crossing the SC and the BM in the middle of their entrance window. On the right, the aluminum box that encapsulates the target holder and the vertex detector is shown.

The efficiency [20] showed an excellent stability during the whole data taking, with a measured mean value of (99.7±0.15)%. A good performance was also observed for the time resolution (σ_t), with a measured average value of $\sigma_t \approx (150 \pm 2)$ ps, where marginal fluctuations (maximum ≈ 5 ps) were observed.

B. Beam Monitor Detector

The BM, described in detail in [20] and shown in Fig. 2, is a drift chamber designed for charged particles trajectory reconstruction. This detector is used to measure the ion impinging point on the target, a crucial information needed to address the pile up ambiguity in the VTX detector (see II C 2).

The detector is made of twelve alternated horizontal (along x axis) and vertical (along y axis) wire planes. Each plane is composed of three rectangular cells centered around the sense wires, with dimensions x(y)×z = 16 mm×10 mm, for a total of 36 cells/sense wires. The geometrical layout has been optimized in order to minimize ions interactions with the wires still maintaining the required cell resolution. The twelve planes (six on each "view") provide tracking redundancy and ensure a high tracking efficiency and an excellent spatial resolution. The Beam Monitor was operated at 1.8 kV with an Ar/CO_2 (80%/20%) gas mixture, at atmospheric pressure.

The detector tracking algorithms have been presented elsewhere (in Ref. [20]): the tracking calibration has been performed using the tracks reconstructed in the VTX detector in a dedicated run in which the target was removed, thus allowing the detector alignment and the track intercalibration.

The chamber hit detection efficiency was measured to be ∼97% and was stable during the run as shown in Fig.3 (black triangles) with the largest variation of ∼3%. The mean track spatial resolution at the chamber center was measured to be $\sigma_x \approx$140 µm, with the dependence on the distance from the cell center described in [20].

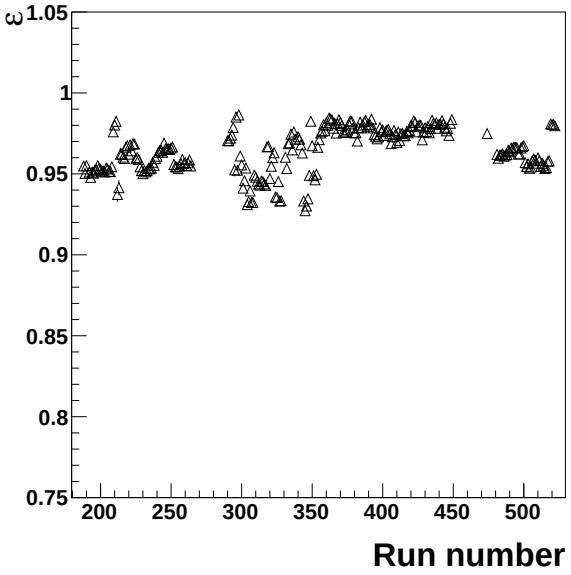

FIG. 3. Beam monitor tracking efficiency as a function of run number. The small fluctuations (≤3%) that can be observed against the mean value of 96.8% is due to the changes in the beam position, as well as to changes in the temperature and pressure of the gas mixture.

C. Vertex Detector

The main purpose of the vertex detector (VTX) is the trajectory and fragmentation vertex reconstruction of fragments produced in the target with the largest possible angular coverage. The detector has been optimized in order to achieve an angular resolution better than $\sim 0.3°$ for the two tracks separation.

The whole detector thickness could not exceed a few per cent of the target thickness to keep the probability of fragmentation inside the sensors at the few per cent level. A dynamic range from about two MIPs (Minimum Ionizing Particle), for the proton signal, to the two or three order of magnitude larger signal from low kinetic energy ^{12}C ions has also to be considered. To satisfy those requirements the MIMOSA26 (M26) pixel sensor has been chosen to equip the vertex detector with four sensor layers: the best compromise between the need of having a minimal track reconstruction redundancy and the sensor total thickness minimization.

M26 is a sensor chip developed by the Strasbourg group [17, 18] for high energy physics experiments. A sensitive area of 10.6 mm × 21.2 mm is covered by 576 rows and 1152 columns of pixels with 18.4 µm pitch with a read-out time of 115.2 µs per frame.

All the pixels are read-out per column with a row read-out time of 200 ns. At the end of each column a discriminator is used to produce the input to the following zero suppression logic, that removes the empty pixel information and stores the data in two buffer memories. The data is thus sent off chip with two 80 MHz serial differential outputs. Only four discriminator thresholds, each common to 288 discriminators, are provided.

To fit the experimental conditions a custom housing board has been designed with two M26 glued on both sides of a square hole to obtain a sensitive area of $\sim 2 \times 2$ cm^2 including a small superimposition region essential to align all VTX sensors. The use of 1 mm thick PCB (Printed Circuit Board) and low profile components, allowing a distance of two consecutive boards of 2 mm, produces an overall thickness of the four vertex stations of 12 mm, as shown in Fig. 4. In these conditions the angular coverage is ±40°. Finally, the overall thickness of about 50 µm per sensor, allows to minimize the lateral straggling of the impinging particles.

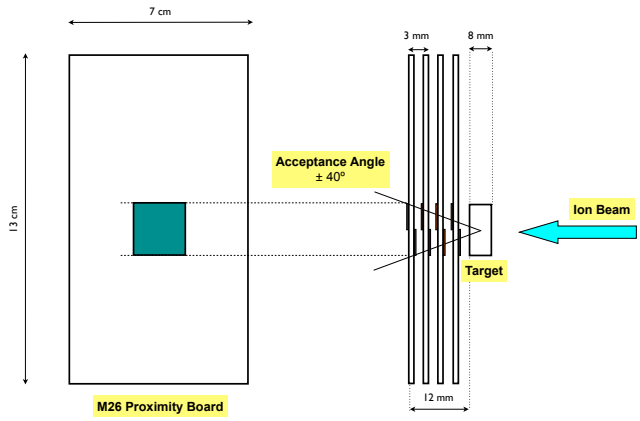

FIG. 4. Sketch of the VTX detector arrangement: the beam is impinging on 8 mm thick carbon target. Each of the four following PCBs is housing two sensors, one on each side, placed over a square hole (2 cm side length) in the PCB itself.

1. *Performances*

The VTX detector data processing proceeds from the raw data file reading, from which a list of fired pixel is extracted, to the clusters reconstruction, centroid evaluation and combination into a list of tracks and vertices. A clustering algorithm is performed for each sensor to reconstruct the crossing point of the ionizing particles going through the M26 sensor. The algorithm is based on a recursive method looking for the next neighboring fired pixel and was able to reconstruct correctly the clusters with an efficiency higher than 99.9% [21].

Tracking reconstruction is based on standard algorithms tuned for the specific applications of CMOS sensors aiming for the reconstruction of a track going from a given plane to the next. Starting from the last plane and proceeding backwards with respect to the beam direction, a road to the position given by the BM extrapolation on the target is defined. Then all the available clusters on each plane within this road are identified and selected. The tracking reconstruction efficiency, evaluated on Monte Carlo simulation events (see § III) is $98.7 \pm 0.1\%$, with a measured proportion of fake tracks of $1.99 \pm 0.01\%$ [21].

Two other different tracking approaches have been implemented and tested to assign a systematic uncertainty on the VTX tracking: one is based on the Hough transformation, while the other implements a different iterative procedure to scan the VTX planes to assign fired pixels to a given track in which consecutive planes are used. In the following, the first algorithm is used for track reconstruction since it is faster and exhibits a lower proportion of fake tracks.

The fragmentation vertices reconstruction is performed using an algorithm based on a probability distribution approach. Using the MC simulation a vertex reconstruction efficiency of $98.6 \pm 0.2\%$, with a proportion of $2.30 \pm 0.01\%$ fake vertices, has been estimated. The resolution of the vertex reconstruction, evaluated using Monte Carlo events, is better than 10 µm in X and Y directions and better than 50 µm in Z direction [21].

More than one ^{12}C ion can impinge on the VTX detector during the M26 sensor integration time of 115 µs (pile-up effect).

Using a Poisson distribution for pile-up events, with a λ parameter determined by data collected with the SC detector, it was found that only in $(2.4 \pm 0.1)\%$ of the events, the vertex reconstruction algorithm could not disentangle the different vertices. From the data we obtain $\lambda = 0.63 \pm 0.12$ where the uncertainty comes from the distribution of the λ values for different data samples. More details about the performance of the VTX detector can be found in reference [21].

The VTX alignment procedure is based on the minimization of the distance between the reconstructed clusters centroid and the intersection of the reconstructed tracks on the plane. The free parameters to be minimized are the displacement in the orthogonal plane with respect to the beam (X-Y plane) and the rotation around the beam axis (Z axis) for each sensor. Other rotations are neglected since the tracking procedure is less sensitive to them. The minimization is stopped once the variation of the displacement and angle is lower than a given value ($\Delta X, \Delta Y < 5$ µm and angle $< 0.1°$). Figure 5 shows the residuals obtained using ^{12}C ions straight track events at 400 MeV/u for X and Y coordinates after the alignment procedure. The residuals are defined as the distance between the cluster positions and the fitted track line: their distribution was used to evaluate the resolution (σ) of the tracking device by means of a Gaussian fit. The resolution in X and Y directions is better than $\sigma = 5$ µm and the fraction of tails outside a 4σ window is smaller than 17%.

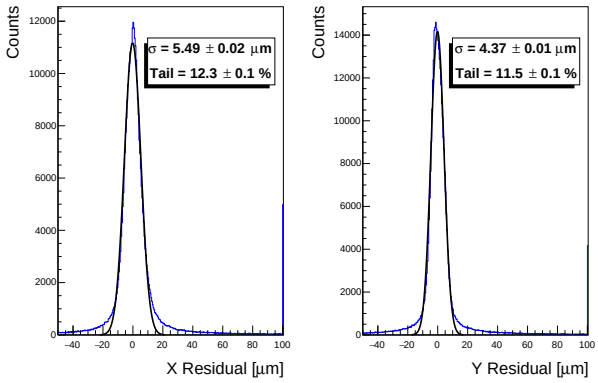

FIG. 5. Residuals obtained for reconstructed tracks in the X (left plot) and Y (right plot) directions. The data distribution is shown in blue, while the result of a Gaussin fit to the histogram is superimposed in black.

2. Matching with the BM

Since the tracks reconstructed by the VTX are the seed for the global track reconstruction algorithm (see § IV), it is crucial to preselect the tracks that belong to each event, getting rid of the piled-up tracks that may have been reconstructed. The ambiguities on which tracks belong to the current event can be resolved by using the information from the BM track, extrapolated to the target since the BM read-out time is fast enough to ensure that tracks belonging to different events cannot be mixed.

The track reconstructed in the BM is used to predict the impact point in the center of the target. The positions of the vertices reconstructed by the VTX for each event are compared with the position predicted by the BM and the closer vertex to the BM is selected as *matched vertex*. The impact of this selection on the final result and the relative systematic uncertainty on the cross section measurement is discussed in § VI.

The BM and VTX detectors were software aligned using calibration events taken without any target, with tracks traversing both detectors without any fragmentation or scattering. The alignment constants were tuned by minimizing the distance between the two predicted track intersections with a virtual plane in the target position (VTX - BM residual distribution) and the difference between the track parameters (like the angle with respect to the beam axis θ). The aligment result is shown in Fig. 6, where a bias in the VTX - BM residual distribution smaller than 200 µm and a resolution of the order of 300 µm for the X coordinate is shown, with similar results for the Y coordinate.

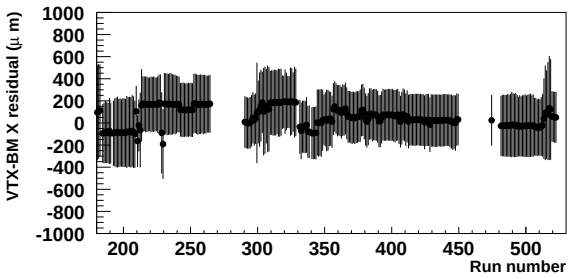

FIG. 6. Mean value of the residuals obtained for the X track at target position as measured using the BM and VTX detectors. The error bars are showing the sigma obtained from a fit done with a Gaussian PDF to the residual distribution and hence are representing the detector matching resolution.

D. ALADIN Magnet

The p/Z ratio of charged fragments is reconstructed using the horizontal deflection in the Large Acceptance DIpole magNet (ALADIN). The magnetic field acts on the particles travelling in the magnet gap, operated in vacuum, that has an approximate volume of $155(H) \times 50(V) \times 230(L)$ cm^3. The magnet angular acceptance is limited to 5.7° by a circular collimator of 15 cm diameter positioned at 75 cm from the target.

The value of the magnet current has been choosen so that a non interacting beam particle crosses the central region of the TW, and it has been kept constant during the data taking within ±0.5%. The corresponding deflection for a 400 MeV/u ^{12}C ion is 5.3°.

The values of the magnetic field used in the reconstruction and simulation comes from interpolation of maps measured at GSI along the three coordinate axes on about 10^4 grid points for different current values.

The actual current value used for the data analysis ($\sim$ 680 A) is determined with the MC by requiring that a beam particle crosses the TW in the same positions as measured in special runs with and without the magnetic field. The uncertainty on the magnet current and field scale is limited by the TW position resolution and estimated to be 2.5%. The uncertainty on the field scale and on the position of the magnet with respect to the rest of the apparatus is taken into account in the evaluation of the cross section measurement systematic errors.

E. ToF-Wall Detector

The ToF-Wall (TW) detector has the aim of measuring the arrival time, the energy release and the impinging position of ions or fragments produced within the angular acceptance of the ALADIN entrance collimator ($\lesssim 5°$). Moreover, exploiting the information of energy release and arrival time, the TW allows the identification of the particles (incident ^{12}C beam and fragments) arriving on it.

The detector, described in detail in [16], consists of two walls of BC-408 plastic scintillator slats (110 cm long, 1 cm thick) divided in 12 modules of 8 slats each.
The detector is placed at a distance $d \simeq 600$ cm from the target, along the trajectory of the ^{12}C beam. The two walls are separated by 8 cm from each other.
At top and bottom ends of each slat, the signal of the impinging particle is read by two photomultiplier tubes (PMT). The signals are split into two branches, as shown in Fig. (7). The first branch is acquired by FASTBUS Analog-to-Digital Converters (ADC) for charge measurements. The second branch is processed by Constant Fraction Disciminators (CFD) and passes digital delay modules before entering Time to Digital Converters (TDC) that provide the time information.

1. TW calibration

As mentioned before, the TW detector is fundamental in the experiment layout because it measures the horizontal and vertical coordinates (X, Y) of the impact

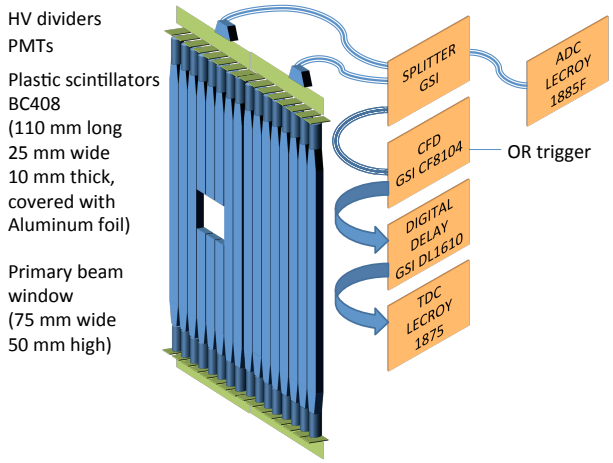

FIG. 7. Sketch of layout and connections of TW scintillator modules and of the read-out eletronics with splitters, constant fraction discriminators (CFDs), digital delays, TDC and ADC boards.

point, the arrival time (ToF) and the energy released in the slats (E_{loss}) of each impinging particle.

In particular, the coordinate in the horizontal plane is related to the slat number, which gives information on the X position of the particle and also on the fired wall (i.e. Z coordinate). The Y coordinate, instead, can be calculated in two ways: either starting from the difference of top and bottom TDC readings or by comparing the signals recorded in the two ADCs. The sum of top and bottom TDC readings, that is independent of the hit-position in the slat, is used to derive the particles ToF. Finally, the ADC channel measurements, providing information on the collected charge, allow to calculate the energy lost by the particle in the slat (E_{loss}). E_{loss} is computed as the geometric mean of the upper and lower ADC and it is independent on the fragment impact position under the assumption of an exponential attenutation of the light in the scintillator.

The calibrations of the quantities of interest have been performed exploiting particular data sets, called "sweep-runs", collected without target, in which the beam conditions were known. In these runs the ^{12}C ion beam (at 400 MeV/u) has been deflected, on the horizontal plane over all the slats, by varying the magnetic field. ^{12}C ions flew at known energy – and thus at known velocity – on tracks which could be reconstructed by geometrical calculations. The hit coordinates (X, Y, Z), ToF and E_{loss} are known on average for sweep-run hits: delays, constant factors and gains can thus be calibrated comparing the measured quantities, with the known values.

In addition to the ToF calibration, a data sample has been collected with dedicated runs in order to take into account the time dependence on the energy released by the fragments in each slat. A scan of the TW with the beam hitting an alluminium bar placed immediately before the scintillator front plane was performed. The time dependence on the released energy (time-walk effect) has been found to be <0.5 ns and thus has been neglected in the TW hit reconstruction.

In calibration data samples, obtained scanning with the primary C ions the TW, the ToF is determined by the known energy (i.e. velocity) and the path length to the individual slats.

The fragment impact vertical position can be obtained by using the ADC or TDC information, respectively. The first possibility is to calculate Y through the ADCs (Y_{ADC}), assuming that an exponential attenuation is responsible of the signal decrease as a function of the lenght traversed along each slat and that the two photomultipliers can have different light gains. The calibration parameters have been measured by using the positions (Y coordinates) of the intercept between the VTX track extrapolation and the TW planes as a reference.

The second possibility is, instead, to use the TDC readings and the light speed in the scintillator (v_{sl}, slat dependent) to compute the Y coordinate (Y_{TDC}): in the sweep-runs, on the horizontal plane taken as a reference, the vertical coordinate is known ($Y = 0$). However this latter method suffer from a bigger uncertainty on the position and is only used for slats in which only one ADC was working.

After the pedestal subtraction, the ADC readings can be related to the scintillation light released by the particle by knowing the attenuation and the gain of the photomultipliers for each slat.

In sweep-runs the C ion energy is known and the energy loss can be evaluated according to the Bethe-Bloch formula. The computed E_{loss} is hence used to calibrate the TW detector parameters, taking also into account the non-linear response of plastic scintillators to the ionization density by applying the semi-empirical Birks' formula [22], with parameters that are determined from the data.

2. *TW efficiency*

The efficiency of the TW for proton detection is limited by the minimum signal needed to trigger the Constant Fraction Discriminators and to digitize the time information in the TDCs.

In order to simulate accurately this effect, for each TW channel the fraction of events with a detected TDC hit is studied as a function of the ADC counts after pedestal subtraction, as shown in Fig. 8 (for slat 33, top). The sharp transition from 0 to 1 (parameterized with a sigmoid fit) corresponds to the minimum ADC counts needed to trigger a TDC hit in each channel. The minimum released energy needed to trigger the TDC in each channel is estimated using the calibration parameters and Birks' factors, and used in the Monte Carlo simulation to discard hits with an energy below threshold.

The minimum TW energy that can be detected in at

least one of the two TDCs depends on the threshold values and on the Y position along the TW, due to the light attenuation along the slats. The energy threshold is below the energy released by a minimum ionizing particle, excluding some regions, expecially close to the impact point of the carbon beam, where there is an efficiency loss for protons of high kinetic energy.

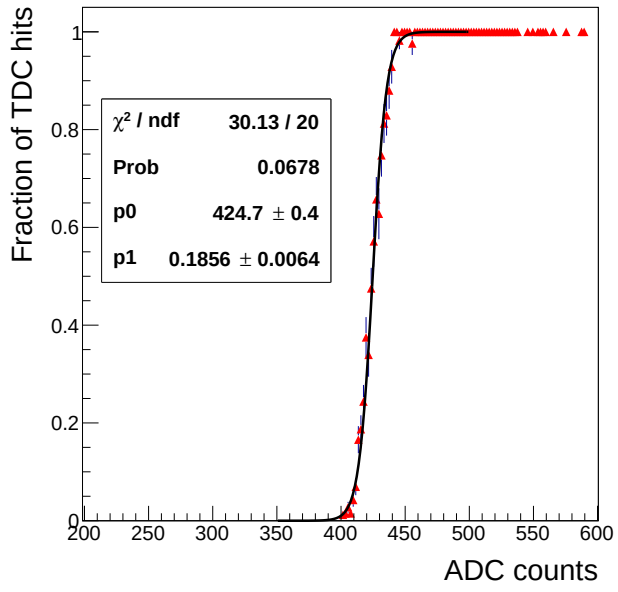

FIG. 8. Fraction of events with a TDC hit as a function of ADC counts for slat 33 of the TW.

3. *TW Resolution*

The resolutions in the TW reconstructed quantites (E_{loss}, Y, ToF) are estimated by comparing the values measured for hits in the two planes compatible with the same particle. The selection of the hits in different planes, optimized using the full Monte Carlo simulation, is based on the geometrical topology of the event and uses as input information the hits slat and Y positions. The resolutions are used for the tuning of the Monte Carlo signal processing.

The Y_{ADC} coordinate resolution was also evaluated using the uncertainty propagation, obtaining similar results. The resolution we found, as expected, depends on the value of the vertical coordinate itself and it is shown as a function of the fragment energy, in Fig. 9 (top, left).

The energy resolution is shown in Fig. 9 (top, right), for data and Monte Carlo as a function of the released energy. The ToF resolution shown in Fig. 9 (bottom, left) is about 800 ps while the Y_{TDC} resolution (bottom, right) is 8 cm and is nearly independent of the energy.

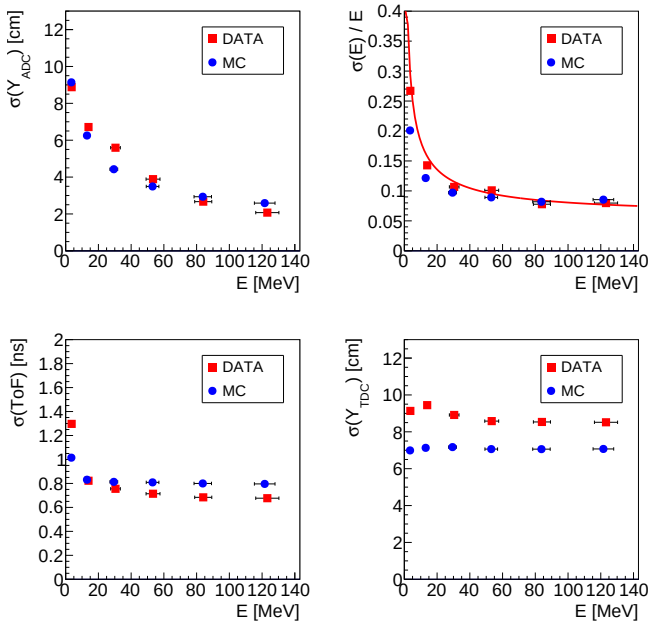

FIG. 9. Top left: Y_{ADC} resolution. Top right: energy resolution. Bottom left: ToF resolution. Bottom right: Y_{TDC} resolution. All the distributions are shown for data (red squares) and MC (blue circles) event samples as a function of the released energy. A red line, showing a $\propto 1/\sqrt{E}$ distribution is superimposed to the energy resolution distribution.

F. Trigger and DAQ

The read-out of the detector electronics is performed on an event-by-event basis using the Multi Branch System (MBS) [23], a general DAQ framework developed at GSI. For each trigger, the MBS system handles the read-out of the bus controllers hosted in different crates and takes care of the trigger synchronization through signals distributed on a common trigger bus. The event fragments collected from all the individual controllers are transmitted during the beam inter-spill period to a host PC where the data merging and saving is performed.

The signals from single detectors are locally processed with NIM electronics to generate trigger primitives. The final trigger logic is implemented in a FPGA programmable VME module (VULOM4 [24]), where the local trigger primitives are combined in logic matrices. The accepted triggers for different logical conditions are propagated to the read-out electronics via the trigger bus. Different trigger outputs are generated with downscale factors or at random times for calibration purposes, while the main physical trigger is based only on the signal from the SC detector, thus providing an unbiased selection of primary beam particles for the data analysis.

The typical beam rate during the data taking was around 1 kHz, with instantaneous fluctuations related to the spill structures provided by the SIS. The mean acquisition rate was 150 Hz due to the dead times of the

single read-out nodes.

III. DATA SAMPLE AND MC SIMULATION

The collected data sample of ^{12}C ions collisions on the thin carbon target corresponds to 24 milion unbiased triggers, while 4.5 milion events have been collected with the thin gold target.

The simulation of the experiment is based on the general purpose Monte Carlo (MC) code Fluka [25, 26], used with the "HadronTherapy" physical model, which includes accurate simulation of non-elastic hadronic interactions at low energy and the evaporation and radioactive decays of heavy fragments.

The detector geometry and materials are modeled in a considerable detail, to properly evaluate the interactions in all the active detectors and the production of secondary particles in out-of-target fragmentation processes. The absolute positions of the detectors in the experimental area are fixed on the basis of the optical survey measurements results performed at the end of the data taking, complemented with alignment studies from the collected data.

The comparison of E_{loss}, ToF and Y coordinate measured from the TW detector for DATA and MC events in which a fragmentation occurred are shown in Fig. 10, where the distributions have been normalized in order to have the same integral. The fragmentation events are defined as those in which at least one vertex has been reconstructed in the VTX detector and more than one track is associated to it. The energy loss distribution for data is shown up to 100 MeV for fragments with Z ranging from one to five, since energy releases above 100 MeV are related to carbon ions. A detailed discussion on the charge identification of the fragments on the basis of energy loss and time of flight can be found in § IV A.

The pile-up of VTX tracks from different primary particles is simulated by adding additional tracks from events stored in a software FIFO, according to a trigger-conditioned Poissonian distribution determined from a data sample, with $\lambda = 0.76$ (to account for the large pile-up condition measured in some data acquisition runs). The distributions of the number of vertices reconstructed with the VTX detector in data (for a large pile up run) and Monte Carlo simulation are compared in Fig. 11.

The detailed MC simulation of the geometry and of the detector response is needed to evaluate the acceptances and resolutions for the cross section measurement. For this purpose each reconstructed track is associated with a MC generated track and the reconstructed variables (kinetic energy, mass, charge, emission angle, momentum) are compared with the corresponding true value at generator level. A MC sample of 105 million events of ^{12}C ions interactions with a carbon target has been used for this purpose: the tracking resolutions and efficiencies as well as a study of the combinatorial and misidentification background contamination in the fragments reconstruction have been performed on this sample (see § IV C).

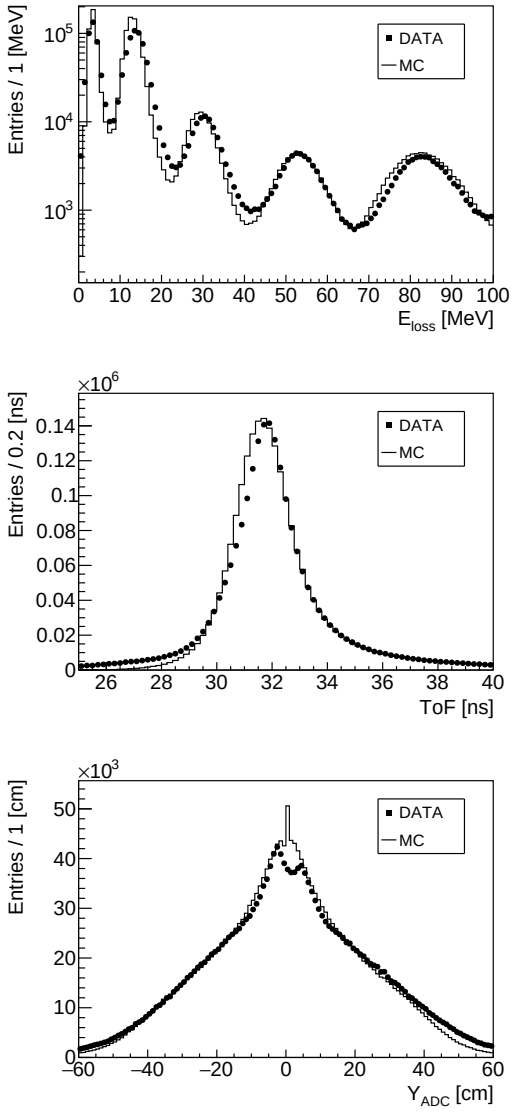

FIG. 10. Comparison of data and Monte Carlo distributions for TW reconstructed variables in fragmentation events. The data and MC spectra have been normalized in order to have the same integral.

IV. GLOBAL RECONTRUCTION

The fragment reconstruction in FIRST proceeds along two possible strategies, accordingly to their production angle: for small angle production (polar angle θ less than $\sim 6^\circ$) the fragment enters the ALADIN magnet region, where the momentum is computed measuring the bending in the x–z plane, and is then detected by the TW; for large angle production (θ larger than $\sim 6^\circ$), the fragments

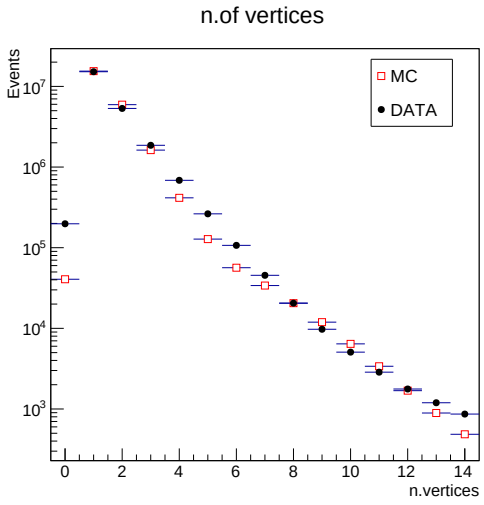

FIG. 11. Number of reconstructed vertices for DATA and MC. The MC distribution is normalized to the same number of entries of the data.

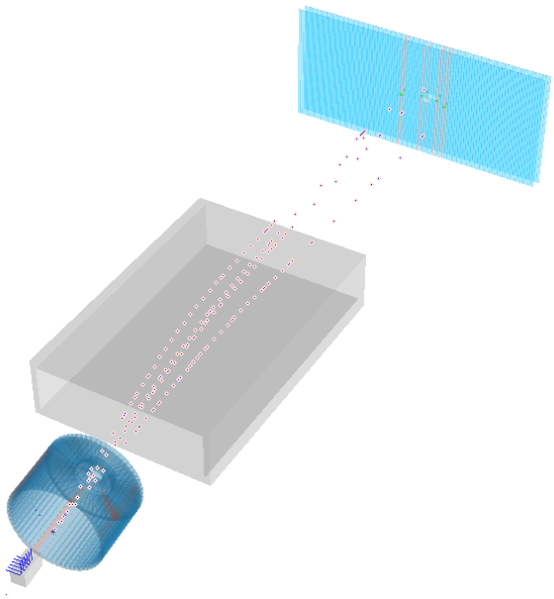

FIG. 12. 3D view of a fully reconstructed fragmentation event, with four fragments produced in the small angle region. Fragment tracks are built by pairing tracks reconstructed in the VTX detector (not shown in this figure, as the scale is too large) with the TW hits detected by the TW (shown in green in the top right light blue region that represents the TW). The tracks are represented as dots connecting the target/VTX region with the green dots on the TW. The magnet region is represented as a grey box between the KENTROS detector and the TW.

cannot enter the magnet region and hence are detected by the KENTROS calorimeter.

The data analysis presented here covers only the small angle production region: fragments are reconstructed, in this case, using an iterative procedure that matches the VTX tracks and TW hits detected in each event. An example of a fully reconstructed fragmentation event, in which four fragments are produced at small angle, is shown in Fig. 12. The fired BM wires/cells are highlighted in blue in the grayish box in the bottom left corner of the picture. The KENTROS blue barrel and endcap modules, surrounding the target/VTX region (not visibile in this global view scale) are shown as well. The fragment tracks are represented as "dots" in space connecting the target origin position, and the relative four fragment tracks in the VTX, with the four pairs of red bands on the TW (two for each fragment as it traverses both the front and the rear wall) representing the TW slats that have been hit. The TW hits used to build the track are shown as tiny spots in green.

The tracks bending happens in the grey box, representing the ALADIN magnet region: before and after that region the magnetic field intensity is negligible and the track trajectory is assumed to be a straight line.

A. Fragment charge identification

In order to fully reconstruct the fragment path and compute its momentum, the fragment charge (Z_{ID}) has to be measured. Two algorithms, based on the informations from the TW and VTX detectors, have been developed.

The TW Z_{ID} identification is performed using the E_{loss} and ToF measurements. The TW performances are good enough to allow the discrimination of six spots in the E_{loss}-ToF plane, related to different fragment charges as shown in Fig. 13. The Bethe-Bloch formula parameters that describe the measured E_{loss} vs ToF distributions are found fitting each spot. Fig. 13 shows the measured distributions for ^{12}C ions on carbon target data, with Bethe-Bloch fitted curves superimposed in black.

The TW Z_{ID} algorithm assign to a given fragment the charge that minimize its normalized distance, in the E_{loss}-ToF plane, with respect to the different Bethe-Bloch curves relative to the different Z hypothesis.

The distance is normalized, for each Z hypothesis, to the σ_{dist} of the distribution obtained from a Gaussian fit to the distance of each hit to each Bethe-Bloch curve measured in the full data sample. Furthermore, the μ_{dist} from the fit is used to unbias the normalized distance distribution.

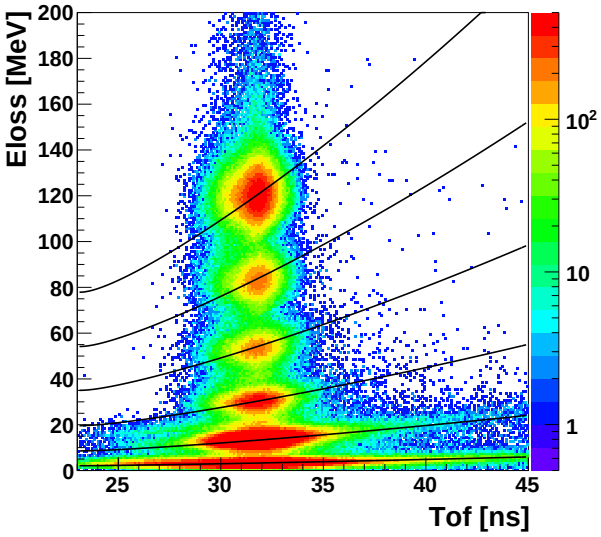

FIG. 13. Measured E_{loss} vs ToF distribution, for all the TW hits reconstructed in the full data sample. The Bethe-Bloch formulas fitted on the data sample are superimposed in black.

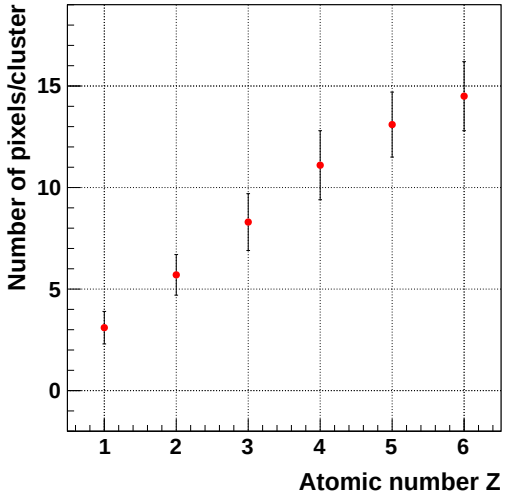

FIG. 14. VTX tracks mean cluster size (number of pixels per cluster) as a function of the fragment charge assigned from the TW Z_{ID} algorithm in a clean sample of global reconstructed tracks.

The VTX detector identification algorithm exploits the correlation between the size of the hit clusters and the fragment charge, as outlined in [27].

The VTX Z_{ID} algorithm has been calibrated on data, using the measured mean cluster size for a given VTX track, as a function of the Z_{ID} returned by the TW detector on a pure sample of global tracks identified applying tight selection cuts. The correlation between these two quantities is shown in Fig. 14.

For each reconstructed track, the VTX Z_{ID} algorithm computes the mean cluster size along the track and uses the calibrated distributions to assign a probability for each Z hypothesis. The hypothesis with the largest probability is then used to assign the Z_{ID} to the fragment.

B. The global tracking algorithm

The global tracking algorithm implements three main steps.

1. First of all the event is pre-selected, applying several filters: at least one hit on the TW and one track in the VTX detector have to be reconstructed; if more than one vertex is found in the VTX detector, the one closest to the BM extrapolated *on-target* position is taken as the true vertex for the event under study, while the others are discarded as PU vertices; only hits on the TW for which a charge assignement was possible are considered (see § IV A); only VTX tracks that are in the ALADIN magnet window entrance acceptance are considered.

2. For all the preselected events an iterative scan of the matching between VTX tracks and TW hits is performed, producing a list of global track candidates. Each track from the VTX is paired with each hit from the TW: clustering of TW hits is done afterwards, when the candidates are ranked and combined. For each candidate a minimization algorithm determines the optimal value of pc/Z and find the corresponding trajectory that matches the VTX track before the magnet and the TW hit.

3. The track candidates are finally combined and ranked accordingly to the VTX-TW matching quality. Duplicated tracks in which the same fragment has produced an hit in both front and rear TW walls are selected according to geometrical and energetic criteria and properly combined. A scoring function to select the best candidates is then applied to the purged list. The resulting track list, in which each VTX track is used to build only one global track, is then used as input for the cross section measurements.

The scoring algorithm combines the information from the VTX and the TW detectors to select the best track candidates. The quantities used to weigh each VTX track / TW hit pair are: the difference between the VTX and TW Z_{ID} (Δ_{Chg}) and the difference between the Y position as extrapolated from the VTX and as measured with the TW (Δ_Y). The adopted scoring function is $\sqrt{\Delta^2_{Chg} \cdot Chg^2_W + \Delta^2_Y \cdot Y^2_W}$. The Chg_W and Y_W weights have been optimized using the full MC simulation by minimizing the fraction of reconstructed background tracks. An example is shown in Fig. 15 for H and He fragments:

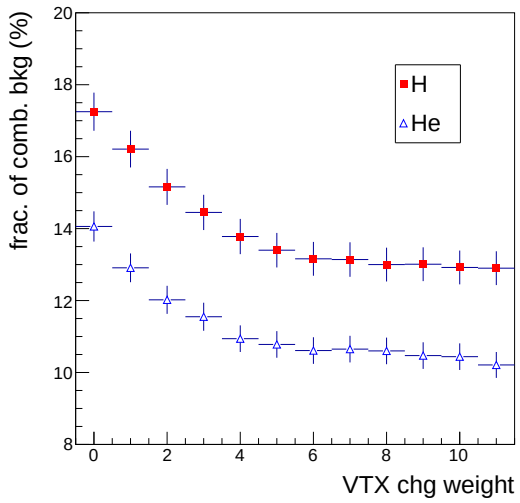

FIG. 15. Optimization of the Chg_W weight, based on the TW and VTX charge identification criteria, in the reconstruction. the fraction of tracks in which The VTX track and the TW hits are not correctly paired with respect to the total number of reconstructed tracks is shown as a function of the weight.

the fraction of tracks in which the VTX track and the TW hits are not correctly paired with respect to the total number of reconstructed tracks is shown as a function of the charge weight Chg_W. The final Chg_W value chosen for the fragments reconstruction is eight.

For each selected global track candidate, all the measured quantities are computed: the charge and the ToF are measured by the TW (for details see § IV A); the particle path (L) and the momentum over charge ratio (pc/Z) are determined by the tracking algorithm, allowing a measurement of the fragment speed (β defined as L/ToF); the mass is computed as $p/(\gamma \cdot \beta)$. The quantities used to build the single differential cross sections are respectively the fragment normalized kinetic energy (E_{kin}/u), computed as the total fragment kinetic energy divided by the atomic number, and the fragment production angle (θ) with respect to the beam axis, measured using the tracks reconstructed by the VTX detector.

C. Tracking algorithm performances

The global reconstruction algorithms have been benchmarked against the full MC simulation (see § III). The angular and kinetic energy resolutions have been measured in order to evaluate possible bias introduced by the reconstruction and to optimize the binning adopted for the SDCS measurement. The tracking efficiency and the background characterization have been performed on the full MC simulation as well. The observed discrepancies between the collected data and the MC simulation have been taken into account when assessing the systematic uncertainties on the result.

1. Angular resolution

The angular resolution has been measured using global tracks from the full MC sample and it has been determined comparing the true fragment direction at the target exit point with the one reconstructed by the FIRST tracking algorithm. The resolution is found to be stable against the track angle, as shown in Fig. 16 with mean values that are in the range 0.054° (for carbons and borons) to 0.076° (for protons). Such numbers are entirely dominated by the intrinsic resolution of the VTX detector.

When comparing the reconstructed fragment direction with the generated value, computed inside the target, the resolution value is instead in the 0.1–0.15° range, being completely dominated by the multiple scattering and depending on the fragment charge and energy.

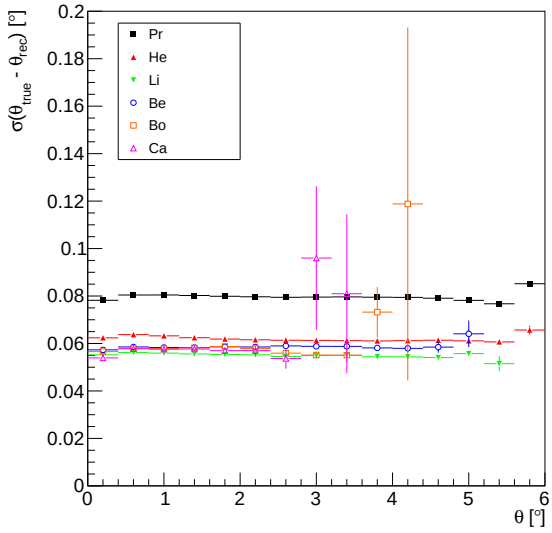

FIG. 16. Angular resolution as a function of the fragment azimutal angle.

2. Normalized kinetic energy resolution

The kinetic energy resolution (σ_{Ekin}) has been measured using global tracks from the full MC sample.

In the σ_{Ekin} distribution two main event categories can be identified: the events in which the tracks are built using the correct combinations of VTX track and TW hits and the events in which the VTX and TW candidates were not correctly paired. The reconstrution biases, as well as the resolutions, measured for the two categories are significantly different, as shown in Fig. 17 for H fragments.

The reconstruction efficiency and resolutions are estimated using the correctly paired tracks, while the

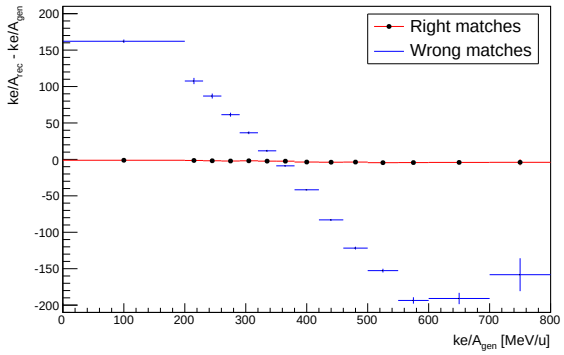

FIG. 17. Reconstruction biases (mean difference between generated and reconstructed values) in E_{kin}/u for H tracks with correct and wrong VTX/TW matches.

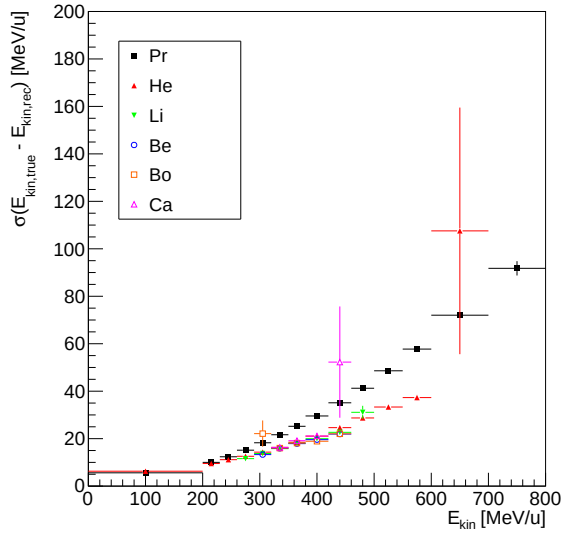

FIG. 18. E_{kin}/u resolution for fragments with different Z_{ID}, from a global track MC sample selected requiring only correctly paired VTX tracks and TW hits.

wrongly paired one is used to model the combinatorial background as discussed in § IV D.

Fig. 18 shows the different fragments E_{kin}/u resolution: the resolution linear dependence on the measured E_{kin}, due to the E_{kin} dependence on the fragment momentum, is observed for all fragments. The computed mass resolution, for the different fragment Z_{ID}, varies in the 0.05–0.2 (GeV/c^2) range for H fragments, increasing up to 0.3–0.5 (GeV/c^2) for carbons.

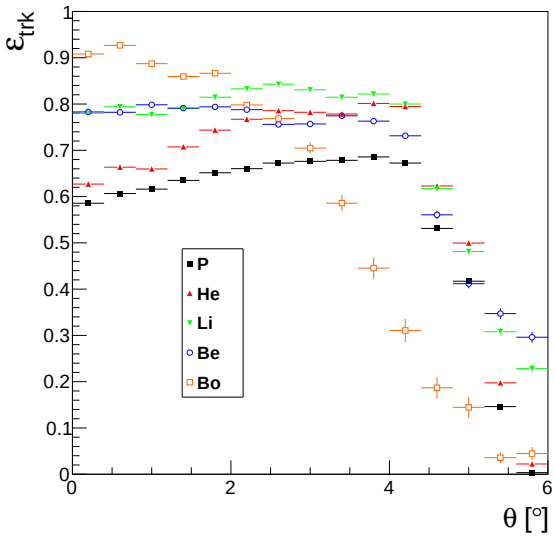

FIG. 19. Tracking efficiency (ε_{trk}) as a function of fragment measured angle θ.

3. *Tracking efficiency*

The tracking algorithm efficiency has been evaluated using the full MC simulation sample (see § III). For charged fragments emerging from the target region, that are additionally required to point inside the geometrical acceptance of the ALADIN magnet ($n_{\rm PROD}$), a check is performed to look for a reconstructed global track that is built using the true TW hit and VTX hits belonging to the true MC tracks under study ($n_{\rm REC}$). The efficiency is hence defined as $\varepsilon_{trk} = n_{\rm REC}/n_{\rm PROD}$ and it is shown in Fig. 19 as a function of the measured angle θ. The uncertainties shown are statistical only.

The drop observed around 5° is due to the geometrical acceptance of the ALADIN magnet entrance window. The tracking efficiency obtained as a function of θ and E_{kin}/u has been used to compute the SDCS as defined in Eq. 1.

D. Combinatorial background evaluation

When pairing VTX tracks and TW hits, as described in § IV B, one has to account for wrong matches or matching between background hits and/or fake tracks forming a random combination that is selected by the scoring algorithm. Such fragments are defined as "combinatorial background", since they represent the result of a reconstruction that artificially pairs (combines) tracks and hits not belonging to a true, common fragment.

The mass spectra of such candidates have to be measured and properly taken into account when measuring the fragment production yields. Fig. 20 shows, for the full MC sample, the mass spectra for two different kinetic

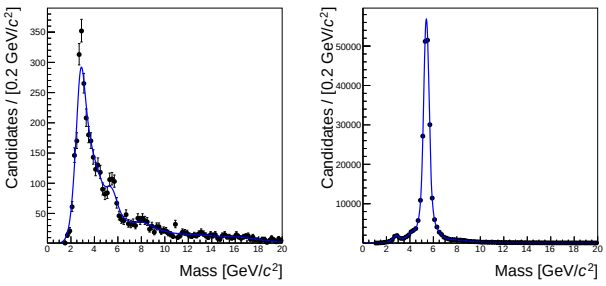

FIG. 20. Mass distribution for two different kinetic energy ranges, 200-230 MeV/u (left) and 350-380 MeV/u (right), for fully reconstructed Li fragment candidates in the full MC sample.

energy ranges (200-230 MeV/u and 350-380 MeV/u) for fully reconstructed fragment candidates selected requiring, at MC truth level, that the VTX tracks and the TW hits used to build the track are belonging to two different particles.

In Fig. 20 the probability density function (PDF) used to model the combinatorial background in the unbinned likelihood fits is shown, as a blue curve, superimposed to the reconstructed mass spectra (black dots). The PDF is built from the measured spectra using the one dimensional kernel estimation method [28] provided by the RooFit package [29].

The uncertainties related to the combinatorial background mass spectra modeling had to be taken into account when fitting the data distributions: the systematic uncertainty affecting the cross section measurement is discussed in § VI.

E. Cross feed evaluation

The limited precision of the Z_{ID} algorithm described in § IV A implies that some fragments are assigned a wrong charge, biasing the final cross section measurement. To properly correct for the cross feed between fully reconstructed fragments, a method based on the full MC sample information has been developed.

The effect due to the wrong Z_{ID} reconstruction is shown clearly in Fig. 21, where the reconstructed mass spectrum is shown for fragments in which Z_{ID}^{rec} is equal to three. The total spectrum is shown in black (solid line). The contribution from the combinatorial background (see § IV D) is shown in red full squares, while the main signal contributions to the spectrum, respectively from ^{6}Li, ^{7}Li and ^{8}Li are shown as open marks (circle, square and triangle respectively). A clear contamination from ^{4}He appears (in blue full triangles), under the ^{6}Li peak: such contamination cannot ben distinguished by the mass fit machinery (the slight shift in central mass value cannot be used in data due to the poor mass resolution) and hence has to be properly subtracted from the fitted yield (Y_i^{raw} in § V).

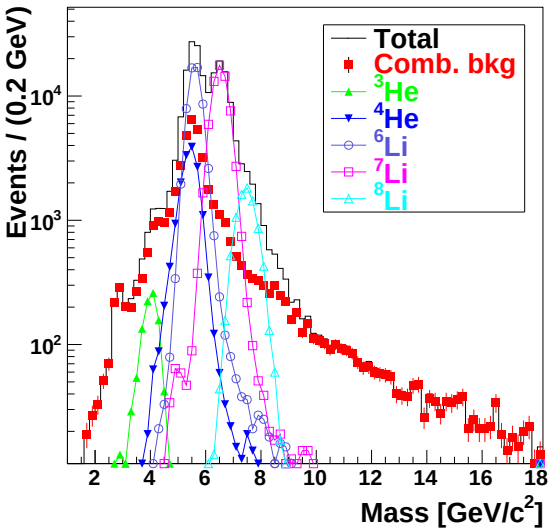

FIG. 21. Reconstructed mass spectrum for Li fragments using the full MC simulation sample. The black spectra is the total reconstructed spectrum. The red full squares are showing the combinatorial background contamination. The main signal contributions to the spectrum, respectively from ^{6}Li, ^{7}Li and ^{8}Li are shown as open marks (circle, square and triangle respectively). The cross feed background from ^{3}He and ^{4}He is shown in full triangles (green and blue, respectively).

To compute the correction factors ε_i^{xf} that have to be applied to the Y_i^{raw} reconstructed yields for each isotope, we have analyzed the full MC sample, in bins of reconstructed angle and kinetic energy and computed the contaminations relative to signal and cross feed isotopes that have nearly the same mass shape. While the absolute amount of a given contamination under a certain reconstructed peak depends clearly on the absolute fragmentation cross section implemented in the MC, the cross feed contamination is a relative correction that depends on the capability of the MC simulation to reproduce the ratio between the different cross sections.

We have therefore corrected the ε_i^{xf} factors in order to take into account the difference in ratio of the integrated cross sections between data and MC: the change in each isotope total cross section measured without any correction applied has been used to assign a systematic uncertainty (see § VI).

F. Kinetic energy distribution unfolding

The resolution study discussed in § IV C and presented in Fig. 18, showed that the kinetic energy resolution degrades, as expected, linearly with the fragment kinetic energy. In order to correct the measured energy for this resolution effect, whose main impact on the result is to broaden the kinetic energy distribution, and to gain access to the fragment true production kinetic energy, an

unfolding procedure has been setup using the TUnfold package of ROOT [30].

The access to the true production E_{kin}/u is particularly important when applying the tracking efficiency corrections (see § V, Eq. 1) to the measured yields, since those corrections are computed as a function of the true production energy. The biased MC simulation has been used for this purpose: a sample of 10 M events for each isotope has been generated with FLUKA shooting directly from the target itself a fragment with a flat production E_{kin}/u spectrum in the range 0–0.8 GeV/u. Using the MC simulation it is possible to build the 2-dimensional unfolding matrix that holds the information needed to translate the measured energy in a production energy measurement. The details on the unfolding algorithm are given elsewhere [30].

For the FIRST application, we used a *kRegModSize* regularization method with regularization strenght τ and binning optimized on the full MC samples by minimizing the chisquare between the unfolded (measured) spectrum and the true (generated) one. While the measured distribution uses 26 bins in the 0–800 MeV/u energy range, with a finer binning in the spectrum central region, the unfolded distribution uses 15 bins as required by the unfolding algorithm (coarser binning in the unfolded distribution).

V. CROSS SECTION MEASUREMENTS

The fragment production double differential cross section, as a function of the normalized kinetic energy (E) or angle with respect to the beam axis (θ), is defined as:

$$\frac{d^2\sigma_i}{dE, d\theta} = \frac{Y_i}{N_{^{12}C} \times N_{t,S} \times \Omega(ph.sp.) \times \epsilon_{trk}(E,\theta)} \quad (1)$$

where Y_i is the number of reconstructed fragments that have a atomic and mass number, $N_{t,S}$ is the number of particles in the target per unit surface, $N_{^{12}C}$ is the number of ^{12}C ions impinging on the target, ϵ_{trk} is the tracking reconstruction efficiency (defined in § IV C 3) and $\Omega(ph.sp.)$ is a numerical factor accounting for the phase space relative to a given angular and kinetic energy bin.

The target particles per unit surface are measured, for the FIRST experimental setup, as $N_{t,S} = (\rho_{tgt} t N_a)/A$ where the target density (ρ_{tgt}) was measured to be 4.25±0.01 g/cm^3, the target thickness (t) was 8.07±0.01 mm and N_a and A are the Avogadro number and the carbon atomic number respectively.

The phase space factor ($\Omega(ph.sp.)$) is defined, accordingly to the angular ($BW_\theta = \theta_{max} - \theta_{min}$) and kinetic energy range ($BW_E = E_{max} - E_{min}$) of the selected fragments, as $\Omega(ph.sp.) = (E_{max} - E_{min}) \cdot 2\pi \cdot (cos(\theta_{min}) - cos(\theta_{max}))$. When the integrated SDCS are computed, either integrating on E or θ, the corresponding $\Omega(ph.sp.)$ is computed as either $2\pi \cdot (cos(\theta_{min}) - cos(\theta_{max}))$ or $(E_{max} - E_{min})$. The size of BW_E and BW_θ windows used to display the results have been chosen to be larger than the measured resolutions (see § IV) in order to limit the migrations of the fragments between the different bins.

The number of ^{12}C ions impinging on the target ($N_{^{12}C}$) has been computed counting the physics, unbiased, triggers (see § II F). The occurrence of multiple ^{12}C ions in a single event has been measured and found negligible in our data sample: for each trigger we count a single ^{12}C ion crossing.

While the charge of each fragment is reconstructed using either the VTX or the TW detector, the production abundance of each fragment (Y_i^{raw}), as well as the identification of different isotopes for each charge hypothesis is measured using the reconstucted mass spectra.

The Y_i^{raw} yields are measured using an extended unbinned maximum likelihood fit, performed using the RooFit ROOT toolkit [29]. An example of such fits, for fragments of different charge and selected in different E and θ ranges, is shown in Fig. 22: superimposed to the data distribution (black dots), the total PDF is shown (in red) while the signal PDF, modeling the various isotopes, is shown in blue. A magenta dotted line shows the contribution from the combinatorial background.

To model the signal PDFs in a given energy or angle bin we use one Gaussian for each isotope. The background PDF, that is accounting for the combinatorial background, has been described in § IV D and shown in Fig. 20.

Fig. 22 shows the fit results for different charge and E, θ ranges: the top row shows the invariant mass fits to the H fragments spectra in a given bin of angle (left) and energy (right), while the bottom row shows the same information for Li fragments in different angle (left) and energy (right) bins.

The Y_i^{raw} yields from the fit have yet to be corrected for the cross feed contamination (see § IV E), while the combinatorial background is taken into account with a dedicated PDF. We compute the yields used for the cross section calculation as $Y_i = \varepsilon_i^{xf} \times Y_i^{raw}$.

The yields to be used in the SDCS measurement as a function of E_{kin} are then corrected for the kinetic energy resolution effect, as described in § IV F. The *unfolded* yields are the ones used for the SDCS calculation.

The measured SDCS as a function of θ and E_{kin} are shown respectively in Figs. 23 and 24. The uncertainty shown in the plot accounts also for the systematic contribution, computed as described in § VI.

The histograms for each atomic number have been obtained by summing up all the non negligible contributions from different isotopes that have the same Z_{ID}. A full set of tables and plots for all the detected isotopes is provided in the appendix.

VI. SYSTEMATIC CHECKS

Several systematic checks have been performed in order to assess the impact of the detector resolution and

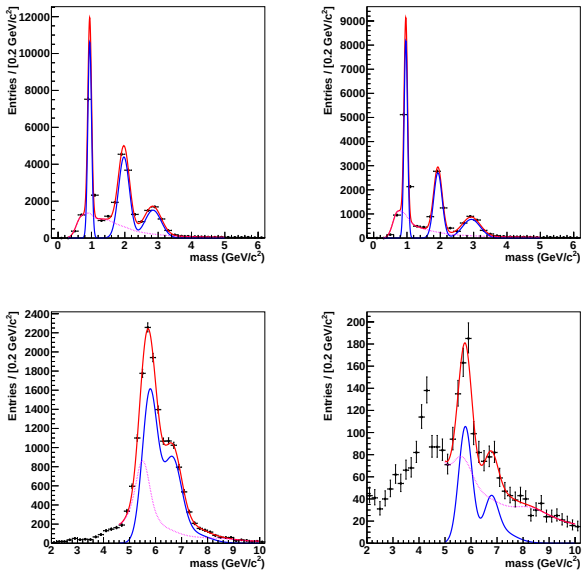

FIG. 22. Fit results for H and Li fragments mass spectra in different E, θ ranges. The top left shows the invariant mass fits for H fragments and angle between 0.4° and 0.8°, the top right for fragments with the same atomic number and a normalized kinetic energy in the range between 200 MeV/u and 230 MeV/u. The bottom left shows the invariant mass fits for Li fragments and angle between 1.2° and 1.6°, the bottom right fragments with the same atomic number and a normalized kinetic energy in the range between 260 MeV/u and 290 MeV/u.

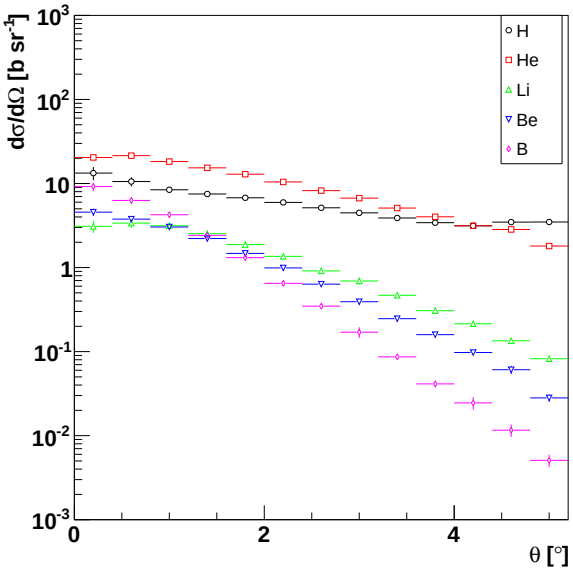

FIG. 23. SDCS of different charge (Z) fragment production, as a function of the fragment angle with respect to the beam axis, computed using Eq. 1.

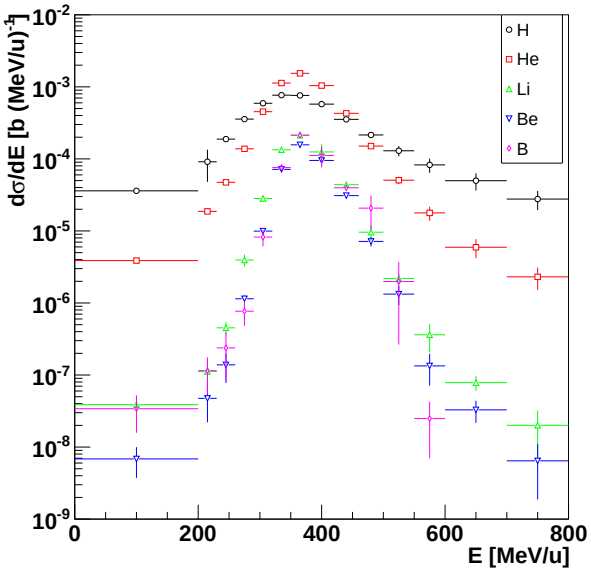

FIG. 24. SDCS of different charge (Z) fragment production, as a function of the fragment normalized kinetic energy, computed using Eq. 1.

discrepancies between data and MC on the SDCS measurements. The analysis has been redone several times, changing the recontruction algorithms, MC samples, measurement strategies: the systematic uncertainty realtive to each measurement has been assigned by looking at the results spread (RMS).

In the following we will refer to the result obtained by following the prescriptions and strategies outlined in the previous sections as the *Default* result.

An important contribution to the systematic uncertainty quoted for the production cross section of H fragments comes from the modeling of the TW hit detection efficiencies. In the TW detector, designed to have a wide dynamic range to detect heavy Z fragments, the H fragments signal is just above the minimum threshold that can be set to have a signal in the CFDs. For this reason, the calibration and use of events in which only one TDC gives a signal when a slat is hit, is important specifically for these fragments. To evaluate the impact of the threshold modeling in our MC simulation we have re-done the analysis rejecting the events in which only one TDC per slat gave a signal: the change with respect to the *Default* is a measurement of the goodness of the MC simulation of our thresholds and the relative hit reconstruction efficiency. The difference observed is, as expected, significant only for protons and is shown, in red full topside down triangles in Fig. 25 (*SCC* spectrum).

The analysis has also been redone by changing both the scoring function, using different Δ_Y and Δ_{Chg} weights, and disabling the TW hits clustering algorithm. The result, for protons, is shown in Fig. 25 (*Cls/Sco*, *Cls/Sco* and *Cls/Sco* spectra) in blue empty circles.

The VTX tracking robustness and the matching of BM

and VTX informations has been checked by changing the reconstruction algorithms and relaxing the requirement of having a BM matched track: the results are shown in Fig. 25 in the *VTX trk* and *BM mat* spectrum. The observed variations, in most bins, are within the statistical uncertainty.

To evaluate the impact on the limited precision of the TW position with respect to the general FIRST reference frame, the TW position in the reconstruction algorithm was changed of about ±1 cm (resolution of the survey performed after the data taking). The result is shown in Fig. 25 spectra labeled as *TW pos+(-)*. A similar study has been done changing the magnet position and the magnetic field scale within the experimental precisions.

The fragments mass spectra data/MC differences had to be taken into account in the Y^{raw} measurement, to avoid any bias in the fit result. We have redone the mass fit study after changing the combinatorial mass model PDF description promoting the detail preservation over the PDF smoothness. The observed result is, for most bins, well within the statistical uncertainty, as shown in Fig. 25 (spectrum labeled *Bkg model*). It has also to be noted that the different analyses strategies tested performing the systematic uncertainty evaluation explored several combinatorial background conditions (modified shapes and different background contamination): the final systematic uncertainty therefore covers also the background contamination subtraction in different background conditions.

The systematic checks include the evaluation of the MC simulation impact on the estimate of the cross feed correction that is used to correct the Y^{raw} yields as presented in § IV E. We have switched off, from the calculation of the correction factors, the data/MC difference rescaling in order to evaluate the maximum impact of this correction.

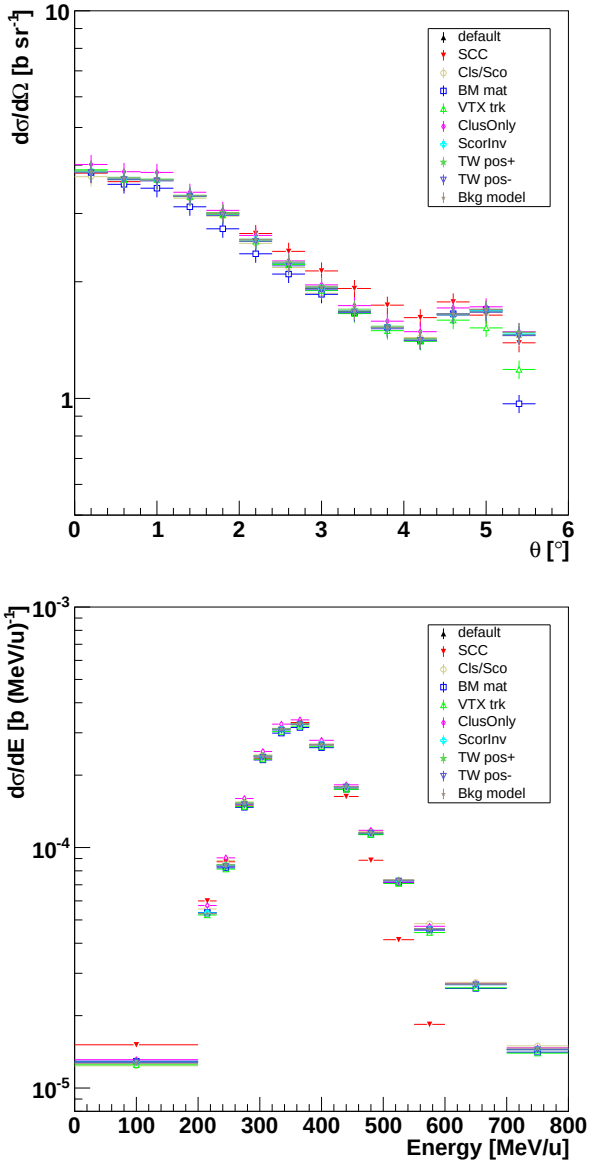

FIG. 25. Effect of systematic checks on the production crossection of ^{1}H fragments. The production cross section obtained changing the analysis strategy, algorithm and cuts is shown. For details on the different spectra labels see the text.

VII. CONCLUSIONS

The FIRST experiment performed a measurement of fragment production SDCS as a function of production angles and kinetic energies, studying a data sample of several million collisions of ^{12}C ions impinging on a thin (8 mm) carbon target. The measurement experimental configuration, as well as the ^{12}C ions energy of 400 MeV/u, allowed to provide results that are particularly interesting for particle therapy and space applications.

The result presented here, while being systematically dominated, are achieving an unprecedented precision on the single differential cross sections of carbon ions on a thin carbon target. While this study covers only a limited angular range (up to five degrees) and reports only the single differential cross sections on the carbon target, a refined analysis, to be performed in the full angular range accessible to the experiment, as a function of E and θ and including the gold target sample, is in preparation.

ACKNOWLEDGEMENTS

We would like to acknowledge M. Arba, L. La Delfa and M. Tuveri (INFN Sez. Cagliari), M. Anelli, S. Cerioni, G. Corradi, D. Riondino and R. Rosellini (INFN, LNF), M. Capponi and A. Iaciofano (INFN, Sez. Roma3) for the technical design and mechanical work on the Interaction Region and Filippo Bosi (INFN Sez. Pisa) for his help and suggestions. We also acknowledge Dr. Håkan

T. Johansson for the invaluable help in setting up the trigger. This work has been supported by the European Community FP7 - Capacities, contract ENSAR n 262010. This work was also supported by Junta de Andaluca and the Spanish Ministerio de Ciencia e Innovación Contracts P07-FQM-02894, FIS2008-04189 and FPA2008-04972-C03.

[1] M. De Napoli *et al.*, "Carbon fragmentation measurements and validation of the GEANT4 nuclear reaction models for hadrontherapy", Phys. Med. Biol. **57** (2012) 7651.

[2] M. De Napoli *et al.*, "Carbon Fragmentation Cross Sections for Hadrontherapy and Space Radiation Protection" Nuclear Data Sheets Volume 119, pages 273-276 (2014)

[3] C. Zeitlin *et al.*, "Fragmentation of 14-N, 16-O, 20-Ne, and 24-Mg Nuclei at 290 to 1000 MeV/nucleon", Phys Rev. C **83** (2011) 034909

[4] C. Zeitlin *et al.*, "Fragmentation cross sections of 290 MeV/nucleon and 400-MeV/nucleon C-12 beams on elemental targets", Phys. Rev. C **76** (2007) 014911.

[5] T. Toshito *et al.*, "Measurements of total and partial charge-changing cross sections for 200- to 400 MeV/nucleon C12 on water and polycarbonate", Phys Rev. C **75** (2007) 054606.

[6] N. Matsufuji *et al.*, "Spatial fragment distribution from a therapeutic pencil-like carbon beam in water", Phys Med. Biol. **50** (2005) 3393.

[7] J. Dudouet *et al.*, "Zero-degree measurements of C12 fragmentation at 95 MeV/nucleon on thin targets", Phys Rev. C **89**, (2014) 064615.

[8] J. Dudouet *et al.*, "Double-differential fragmentation cross-section measurements of 95 MeV/nucleon 12C beams on thin targets for hadron therapy," Phys. Rev. C **88**, 024606 (2013).

[9] M. Durante and F. A. Cucinotta, "Physical basis of radiation protection in space travel.", Rev. Mod. Phys. 83 (2011) 1245-1281

[10] L. Ziwei, "Determination of important nuclear fragmentation processes for human space radiation protection.", Phys. Rev. C 75 (2007) 034609

[11] D. Schardt, T. Elsässer and D. Schulz-Ertner, "Heavy-Ion Tumor Therapy: Physical and Radiobiological Benefits.", Rev. Mod. Phys. 82 (2010) 383-422

[12] J. S. Loeffler and M. Durante, "Charged particle therapy–optimization, challenges and future directions.", Nat. Rev. Clin. Oncol. 10 (2013) 411-424

[13] J. W. Norbury, J. Miller, A. M. Adamczyk, L. Heilbronn, L. W. Townsend, S. R. Blattnig, C. J. Zeitlin (2012), "Nuclear data for space radiation". Radiat. Meas., 47(5), 315363. doi:10.1016/j.radmeas.2012.03.004

[14] K. Gwosch, B. Hartmann, J. Jakubek, C. Granja, P. Soukup, O. Jäkel and M. Martišíková, "Non-invasive monitoring of therapeutic carbon ion beams in a homogeneous phantom by tracking of secondary ions", Phys. Med. Biol. **58** (2013) 3755.

[15] P. Henriquet, E. Testa, M. Chevallier, D. Dauvergne, G. Dedes, N. Freud, J. Krimmer, J. M. Létang, C. Ray, M-H. Richard and F. Sauli, "Interaction vertex imaging (IVI) for carbon ion therapy monitoring: a feasibility study", Phys. Med. Biol. **57** (2012) 4655.

[16] R. Pleskac *et al.*, "The FIRST Experiment at GSI", Nucl. Instr. Methods in Phys. Res. A, Vol. 687 (2012) 130.

[17] http://www.iphc.cnrs.fr/-CMOS-ILC-.html

[18] Ch.Hu-Guo et al., Nuclear Inst. and Methods in Physics Research, Vol. 623, (2010), p. 480-482

[19] C. Sfienti *et al.*, Proceedings of the XLI International Winter Meeting on Nuclear Physics, Bormio, Italy, (2003), p. 323.

[20] Z. Abou-Haidar *et al.*, "Performance of upstream interaction region detectors for the FIRST experiment at GSI," JINST **7**, P02006 (2012).

[21] R. Rescigno *et al.*, "Performance of the reconstruction algorithms of the FIRST experiment Pixel Sensors Vertex detector", Nuclear Inst. and Methods in Physics Research A, Vol. 767, (2014), p. 34-40

[22] J. B. Birks, "Scintillations from Organic Crystals: Specific Fluorescence and Relative Response to Different Radiations", Proc. Phys. Soc. A 64 874 (1951)

[23] H. G. Essel, N. Kurz, IEEE Transactions on Nuclear Science NS-47 (2) (2000) 337.

[24] https://www.gsi.de/informationen/wti/ee/elekt_entwicklung/vulom_m_e.html

[25] G. Battistoni *et al.*, "The FLUKA code: Description and benchmarking", Proceed. of the Hadronic Shower Simulation Workshop2006, (2007), aIP ConferenceProceed. 896(2007)3149.

[26] A. Ferrari, P. R. Sala, A. Fassó, J. Ranft, "FLUKA: a multi particle transport code", Tech. Rep. CERN-2005-10, INFN/TC05/11, SLAC-R-773 (2005).

[27] E. Spiriti *et al.*, "The FIRST experiment: interaction region and MAPS vertex detector", Nucl. Phys. B (Proc. Suppl.) **215** (2011) 157161.

[28] K. S. Cranmer, "Kernel Estimation in High-Energy Physics", Computer Physics Communications 136:198-207,2001. e-Print Archive: hep ex/0011057

[29] W. Verkerke and D. P. Kirkby, "The RooFit toolkit for data modeling," arXiv:physics/0306116.

[30] S. Schmitt, "TUnfold: an algorithm for correcting migration effects in high energy physics", JINST **7** (2012) T10003 [arXiv:1205.6201].

TABLE I. Angular Differential Cross Section [b sr^{-1}]

θ [deg]	^{1}H $d\sigma/d\Omega[b\ sr^{-1}]$	^{2}H $d\sigma/d\Omega[b\ sr^{-1}]$	^{3}H $d\sigma/d\Omega[b\ sr^{-1}]$	^{3}He $d\sigma/d\Omega[b\ sr^{-1}]$	^{4}He $d\sigma/d\Omega[b\ sr^{-1}]$	^{6}He $d\sigma/d\Omega[b\ sr^{-1}]$
0.2(0.2)	3.8 (0.23)	7.3 (2)	2.8 (0.41)	1.7 (0.32)	19 (1.2)	0.051 (0.071)
0.6(0.2)	3.7 (0.21)	4.5 (1)	2.6 (0.28)	1.8 (0.16)	19 (1.2)	0.28 (0.085)
1(0.2)	3.7 (0.21)	2.7 (0.35)	2.1 (0.24)	1.9 (0.17)	16 (0.99)	0.13 (0.056)
1.4(0.2)	3.3 (0.19)	2.3 (0.2)	1.9 (0.24)	1.9 (0.17)	13 (0.76)	0.17 (0.049)
1.8(0.2)	3 (0.17)	2.2 (0.16)	1.6 (0.15)	1.8 (0.14)	11 (0.6)	0.21 (0.028)
2.2(0.2)	2.6 (0.15)	2 (0.13)	1.5 (0.087)	1.6 (0.12)	8.7 (0.48)	0.12 (0.018)
2.6(0.2)	2.2 (0.13)	1.8 (0.1)	1.2 (0.071)	1.4 (0.09)	6.7 (0.36)	0.087 (0.0083)
3(0.2)	1.9 (0.12)	1.5 (0.084)	1 (0.071)	1.3 (0.079)	5.3 (0.29)	0.045 (0.0075)
3.4(0.2)	1.7 (0.11)	1.4 (0.079)	0.82 (0.066)	1.2 (0.067)	3.9 (0.22)	0.0087 (0.0075)
3.8(0.2)	1.5 (0.1)	1.1 (0.074)	0.72 (0.063)	0.99 (0.056)	3 (0.16)	3.4e-08 (0.0025)
4.2(0.2)	1.4 (0.094)	1 (0.069)	0.64 (0.066)	0.82 (0.045)	2.3 (0.12)	0.012 (0.0041)
4.6(0.2)	1.6 (0.096)	1.1 (0.062)	0.69 (0.06)	0.77 (0.043)	2.1 (0.12)	0.023 (0.0036)
5(0.2)	1.7 (0.1)	1.1 (0.065)	0.7 (0.053)	0.46 (0.029)	1.3 (0.075)	0.017 (0.0031)
5.4(0.2)	1.5 (0.18)	0.89 (0.11)	0.61 (0.085)	0.13 (0.0096)	0.34 (0.021)	0.006 (0.0017)
5.8(0.2)	0.0091 (0.0033)	0.006 (0.0023)	0.003 (0.0014)	0.0014 (0.0005)	0.0018 (0.00062)	0.00046 (0.00023)
θ [deg]	^{6}Li $d\sigma/d\Omega[b\ sr^{-1}]$	^{7}Li $d\sigma/d\Omega[b\ sr^{-1}]$	^{8}Li $d\sigma/d\Omega[b\ sr^{-1}]$	^{7}Be $d\sigma/d\Omega[b\ sr^{-1}]$	^{9}Be $d\sigma/d\Omega[b\ sr^{-1}]$	^{10}Be $d\sigma/d\Omega[b\ sr^{-1}]$
0.2(0.2)	1.1 (0.33)	0.99 (0.4)	0.51 (0.17)	1.9 (0.23)	0.94 (0.37)	2 (0.55)
0.6(0.2)	1.5 (0.15)	1.6 (0.4)	0.18 (0.028)	1.4 (0.12)	1.2 (0.27)	1.2 (0.34)
1(0.2)	1.5 (0.19)	1.4 (0.33)	0.17 (0.032)	1.3 (0.085)	0.93 (0.16)	0.82 (0.19)
1.4(0.2)	1.3 (0.17)	0.96 (0.27)	0.18 (0.032)	1.1 (0.074)	0.69 (0.12)	0.46 (0.099)
1.8(0.2)	1 (0.14)	0.61 (0.19)	0.19 (0.045)	0.82 (0.047)	0.39 (0.054)	0.29 (0.053)
2.2(0.2)	0.8 (0.15)	0.42 (0.18)	0.15 (0.036)	0.61 (0.036)	0.33 (0.03)	0.049 (0.027)
2.6(0.2)	0.49 (0.1)	0.42 (0.1)	0.017 (0.013)	0.43 (0.025)	0.1 (0.027)	0.085 (0.016)
3(0.2)	0.42 (0.097)	0.34 (0.085)	0.01 (0.022)	0.28 (0.017)	0.047 (0.014)	0.048 (0.018)
3.4(0.2)	0.14 (0.066)	0.36 (0.077)	0.0017 (0.012)	0.18 (0.011)	0.02 (0.013)	0.029 (0.014)
3.8(0.2)	0.09 (0.032)	0.22 (0.03)	0.0017 (0.012)	0.13 (0.0082)	0.014 (0.0057)	0.017 (0.0055)
4.2(0.2)	0.065 (0.02)	0.15 (0.022)	0.0082 (0.004)	0.08 (0.0056)	0.017 (0.0045)	0.002 (0.0041)
4.6(0.2)	0.047 (0.014)	0.09 (0.016)	0.0013 (0.0017)	0.054 (0.0049)	0.012 (0.0029)	0.0024 (0.00067)
5(0.2)	0.036 (0.0072)	0.038 (0.0059)	0.0071 (0.002)	0.021 (0.0021)	0.0077 (0.0016)	0.00056 (0.00024)
5.4(0.2)	0.008 (0.0018)	0.0066 (0.0024)	0.00049 (0.00097)	0.0046 (0.00069)	0.00058 (0.00069)	4.4e-11 (9.1e-05)
5.8(0.2)	0.0002 (0.00014)	0.0001 (9.2e-05)	5.1e-05 (6.3e-05)	6e-05 (6.9e-05)	3e-05 (4.8e-05)	3e-05 (4.8e-05)
θ [deg]	^{8}B $d\sigma/d\Omega[b\ sr^{-1}]$		^{10}B $d\sigma/d\Omega[b\ sr^{-1}]$		^{11}B $d\sigma/d\Omega[b\ sr^{-1}]$	
0.2(0.2)	0.066 (0.081)		4.9 (1.6)		4.2 (1.1)	
0.6(0.2)	0.023 (0.015)		0.35 (1.3)		6.1 (1.4)	
1(0.2)	0.063 (0.011)		1.8 (0.56)		2.4 (0.6)	
1.4(0.2)	0.052 (0.022)		0.2 (0.46)		2.2 (0.49)	
1.8(0.2)	0.06 (0.014)		0.81 (0.33)		0.45 (0.32)	
2.2(0.2)	0.033 (0.012)		0.11 (0.059)		0.52 (0.079)	
2.6(0.2)	0.037 (0.0057)		0.083 (0.087)		0.23 (0.091)	
3(0.2)	0.016 (0.0031)		0.11 (0.046)		0.0063 (0.045)	
3.4(0.2)	0.014 (0.0043)		0.052 (0.022)		0.018 (0.02)	
3.8(0.2)	0.0044 (0.0024)		0.035 (0.0053)		0.0042 (0.0024)	
4.2(0.2)	0.0036 (0.0016)		0.018 (0.007)		0.0047 (0.004)	
4.6(0.2)	0.0021 (0.0016)		0.0053 (0.0017)		0.0017 (0.0012)	
5(0.2)	0.0011 (0.00071)		0.0037 (0.00095)		0.00036 (0.00046)	
5.4(0.2)	0.00093 (0.00028)		0.00062 (0.00022)		0.00093 (0.00028)	
5.8(0.2)	0 (0)		0 (0)		0 (0)	

TABLE II. Energy Differential Cross Section [b MeV/nucl^{-1}]

Energy	^{1}H	^{2}H	^{3}H	^{3}He	^{4}He	^{6}He
$[MeV/u]$	$d\sigma/dE[b\ MeV/u^{-1}]$	$d\sigma/dE[b\ MeV/u^{-1}]$	$d\sigma/dE[b\ MeV/u^{-1}]$	$d\sigma/dE[b\ MeV/u^{-1}]$	$d\sigma/dE[b\ MeV/u^{-1}]$	$d\sigma/dE[b\ MeV/u^{-1}]$
100(100)	1.28e-05 (7.44e-07)	1.73e-05 (8.71e-07)	5.43e-06 (2.81e-07)	2.10e-06 (8.61e-08)	1.58e-06 (6.19e-08)	1.94e-07 (4.72e-08)
215(15)	5.33e-05 (2.12e-05)	3.88e-05 (1.53e-05)	1.71e-05 (6.78e-06)	1.01e-05 (4.12e-07)	7.85e-06 (4.17e-07)	9.26e-07 (2.00e-07)
245(15)	8.45e-05 (2.96e-06)	6.37e-05 (3.12e-06)	3.88e-05 (2.90e-06)	2.21e-05 (8.60e-07)	2.35e-05 (1.03e-06)	1.67e-06 (3.68e-07)
275(15)	1.52e-04 (4.05e-06)	1.21e-04 (5.82e-06)	8.25e-05 (5.63e-06)	4.79e-05 (1.77e-06)	8.72e-05 (4.48e-06)	2.51e-06 (7.75e-07)
305(15)	2.40e-04 (5.89e-06)	1.98e-04 (8.20e-06)	1.54e-04 (7.38e-06)	1.01e-04 (3.64e-06)	3.41e-04 (2.07e-05)	4.33e-06 (1.40e-06)
335(15)	3.11e-04 (7.44e-06)	2.52e-04 (7.78e-06)	2.02e-04 (5.27e-06)	1.62e-04 (5.90e-06)	9.39e-04 (3.92e-05)	1.52e-05 (3.34e-06)
365(15)	3.26e-04 (7.02e-06)	2.41e-04 (6.83e-06)	1.95e-04 (3.42e-06)	1.99e-04 (5.65e-06)	1.32e-03 (2.75e-05)	1.78e-05 (4.52e-06)
400(20)	2.68e-04 (5.57e-06)	1.78e-04 (5.95e-06)	1.34e-04 (3.04e-06)	1.62e-04 (3.08e-05)	8.97e-04 (3.51e-05)	8.02e-06 (2.69e-06)
440(20)	1.79e-04 (5.37e-06)	1.07e-04 (6.77e-06)	7.35e-05 (3.87e-06)	8.04e-05 (1.80e-06)	3.45e-04 (6.69e-06)	1.61e-06 (4.78e-07)
480(20)	1.15e-04 (7.92e-06)	6.62e-05 (7.84e-06)	3.96e-05 (4.76e-06)	3.29e-05 (9.80e-07)	1.13e-04 (8.02e-06)	4.79e-07 (2.62e-07)
525(25)	7.30e-05 (9.06e-06)	3.84e-05 (7.19e-06)	2.45e-05 (5.01e-06)	1.19e-05 (6.94e-07)	3.83e-05 (5.52e-06)	5.82e-07 (2.06e-07)
575(25)	4.56e-05 (8.02e-06)	2.43e-05 (5.69e-06)	1.73e-05 (4.63e-06)	1.14e-05 (4.27e-06)	6.29e-06 (3.28e-06)	3.27e-07 (1.41e-07)
650(50)	2.69e-05 (5.92e-06)	1.67e-05 (4.52e-06)	1.02e-05 (2.93e-06)	4.55e-06 (1.80e-06)	1.16e-06 (3.76e-07)	1.15e-07 (5.19e-08)
750(50)	1.45e-05 (3.65e-06)	9.45e-06 (2.85e-06)	6.03e-06 (1.76e-06)	1.73e-06 (7.50e-07)	5.61e-07 (1.82e-07)	4.40e-08 (1.73e-08)
Energy	^{6}Li	^{7}Li	^{8}Li	^{7}Be	^{9}Be	^{10}Be
$[MeV/u]$	$d\sigma/dE[b\ MeV/u^{-1}]$	$d\sigma/dE[b\ MeV/u^{-1}]$	$d\sigma/dE[b\ MeV/u^{-1}]$	$d\sigma/dE[b\ MeV/u^{-1}]$	$d\sigma/dE[b\ MeV/u^{-1}]$	$d\sigma/dE[b\ MeV/u^{-1}]$
100(100)	2.51e-08 (6.98e-09)	1.67e-08 (5.57e-09)	0.00e+00 (7.49e-12)	0.00e+00 (2.05e-09)	4.53e-09 (2.94e-09)	0.00e+00 (2.64e-10)
215(15)	9.01e-08 (3.55e-08)	6.01e-08 (2.81e-08)	0.00e+00 (4.68e-10)	0.00e+00 (2.01e-08)	1.51e-08 (1.32e-08)	0.00e+00 (2.28e-09)
245(15)	2.88e-07 (8.27e-08)	1.14e-07 (3.82e-08)	0.00e+00 (1.81e-09)	0.00e+00 (4.58e-08)	3.45e-08 (2.06e-08)	0.00e+00 (8.54e-09)
275(15)	1.50e-06 (5.84e-07)	7.70e-07 (4.13e-07)	2.73e-07 (1.60e-07)	1.03e-06 (1.32e-07)	1.06e-07 (4.60e-08)	0.00e+00 (8.78e-09)
305(15)	9.78e-06 (2.24e-06)	1.27e-05 (1.43e-06)	7.59e-07 (5.32e-07)	6.74e-06 (8.45e-07)	2.25e-06 (3.35e-07)	4.69e-07 (4.96e-07)
335(15)	5.37e-05 (5.79e-06)	5.88e-05 (6.46e-06)	9.40e-06 (2.34e-06)	3.86e-05 (3.06e-06)	2.12e-05 (1.55e-06)	1.09e-05 (1.32e-06)
365(15)	9.02e-05 (5.79e-06)	9.45e-05 (7.83e-06)	1.69e-05 (2.58e-06)	7.76e-05 (4.50e-06)	5.28e-05 (2.86e-06)	2.79e-05 (4.47e-06)
400(20)	6.86e-05 (1.87e-05)	5.86e-05 (1.72e-05)	1.38e-05 (4.24e-06)	5.69e-05 (2.90e-06)	3.28e-05 (3.28e-06)	9.32e-06 (2.47e-06)
440(20)	2.14e-05 (3.86e-06)	2.32e-05 (4.83e-06)	1.75e-06 (6.88e-07)	2.03e-05 (1.13e-06)	6.11e-06 (7.07e-07)	5.68e-06 (1.47e-06)
480(20)	6.68e-06 (1.57e-06)	6.68e-06 (1.25e-06)	0.00e+00 (8.12e-09)	5.64e-06 (1.93e-06)	9.56e-08 (2.20e-07)	0.00e+00 (2.00e-07)
525(25)	1.32e-06 (2.45e-07)	1.05e-06 (1.65e-07)	0.00e+00 (5.91e-10)	7.93e-07 (3.89e-07)	3.29e-08 (2.92e-08)	0.00e+00 (1.84e-09)
575(25)	1.76e-07 (8.15e-08)	1.17e-07 (8.07e-08)	0.00e+00 (2.17e-11)	5.82e-08 (3.88e-08)	5.82e-08 (3.05e-08)	0.00e+00 (0.00e+00)
650(50)	4.73e-08 (1.37e-08)	3.15e-08 (1.05e-08)	0.00e+00 (3.78e-11)	1.68e-08 (7.66e-09)	1.68e-08 (7.63e-09)	0.00e+00 (0.00e+00)
750(50)	1.54e-08 (8.60e-09)	1.03e-08 (6.63e-09)	0.00e+00 (0.00e+00)	2.59e-09 (2.94e-09)	2.59e-09 (2.94e-09)	0.00e+00 (1.22e-09)
Energy	^{8}Bo		^{10}Bo		^{11}Bo	
$[MeV/u]$	$d\sigma/dE[b\ MeV/u^{-1}]$		$d\sigma/dE[b\ MeV/u^{-1}]$		$d\sigma/dE[b\ MeV/u^{-1}]$	
100(100)	1.53e-08 (1.06e-08)		0.00e+00 (4.87e-09)		0.00e+00 (6.91e-09)	
215(15)	5.11e-08 (4.49e-08)		0.00e+00 (1.48e-08)		0.00e+00 (2.09e-08)	
245(15)	1.17e-07 (8.30e-08)		0.00e+00 (4.19e-08)		0.00e+00 (5.72e-08)	
275(15)	3.58e-07 (1.33e-07)		0.00e+00 (1.15e-07)		0.00e+00 (1.23e-07)	
305(15)	1.27e-06 (4.05e-07)		2.58e-07 (5.52e-07)		6.58e-06 (2.09e-06)	
335(15)	3.13e-06 (2.82e-07)		5.68e-06 (5.82e-06)		6.66e-05 (1.05e-05)	
365(15)	4.13e-06 (4.31e-07)		6.95e-05 (1.50e-05)		1.41e-04 (2.35e-05)	
400(20)	2.62e-06 (7.12e-07)		4.87e-05 (1.36e-05)		7.68e-05 (2.28e-05)	
440(20)	1.38e-06 (3.67e-07)		3.99e-05 (4.31e-06)		3.47e-07 (4.67e-06)	
480(20)	1.72e-06 (6.66e-07)		0.00e+00 (1.07e-05)		0.00e+00 (1.28e-07)	
525(25)	0.00e+00 (2.88e-08)		0.00e+00 (1.71e-06)		0.00e+00 (2.88e-09)	
575(25)	0.00e+00 (0.00e+00)		0.00e+00 (0.00e+00)		0.00e+00 (1.79e-08)	
650(50)	0.00e+00 (0.00e+00)		0.00e+00 (0.00e+00)		0.00e+00 (0.00e+00)	
750(50)	0.00e+00 (0.00e+00)		0.00e+00 (0.00e+00)		0.00e+00 (0.00e+00)	

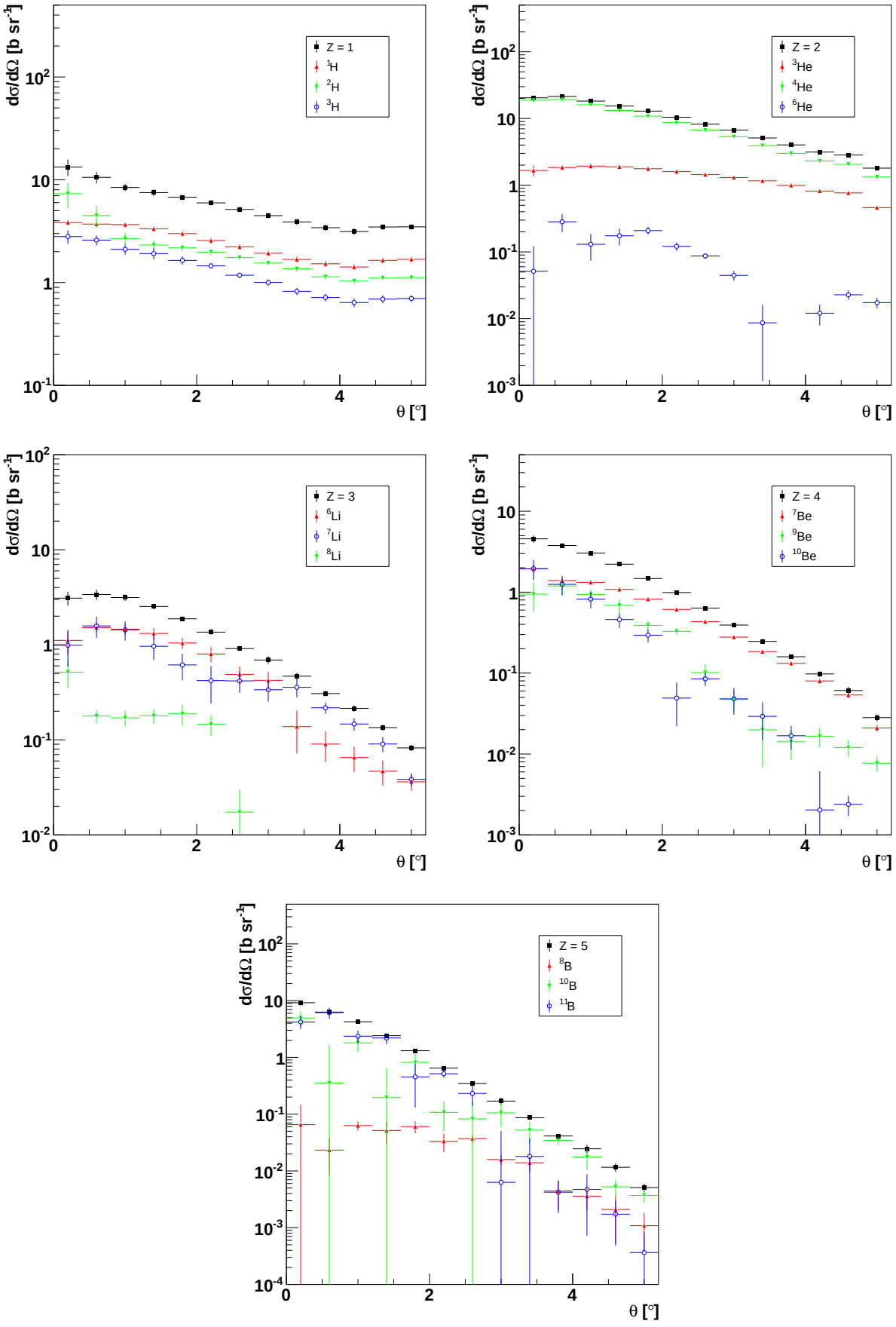

FIG. 26. SDCS of different charge (Z) fragment production, as a function of the fragment angle with respect to the beam axis, computed using Eq. 1. The results for each isotope are shown separately, together with their sum (in black squares).

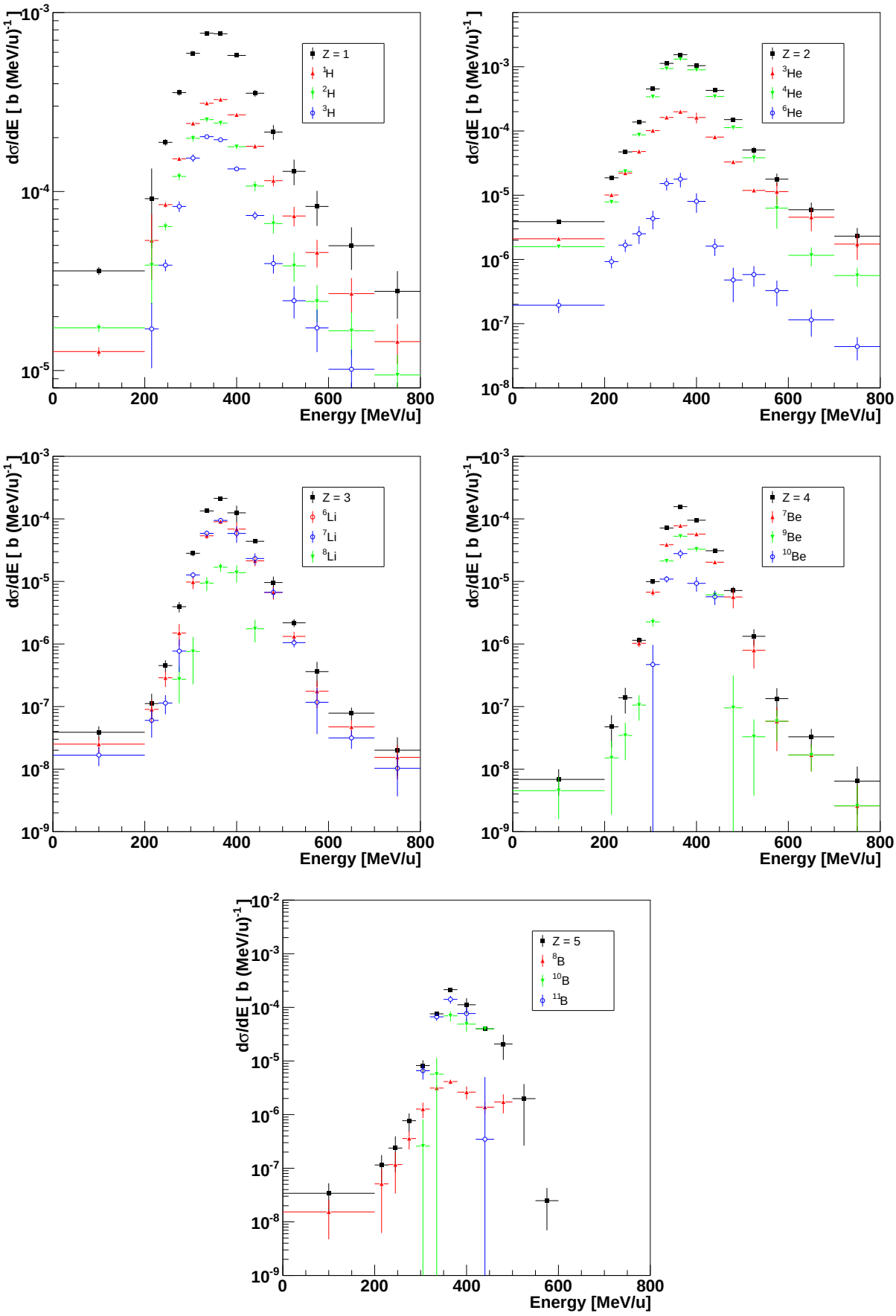

FIG. 27. SDCS of different charge (Z) fragment production, as a function of the fragment normalized kinetic energy, computed using Eq. 1. The results for each isotope are shown separately, together with their sum (in black squares).